JEM Journal of Experimental Medicine

ARTICLE

Immunopathological and microbial signatures of inflammatory bowel disease in partial RAG deficiency

Riccardo Castagnoli[1*], Francesca Pala[1*], Poorani Subramanian[2**], Cihan Oguz[3**], Benjamin Schwarz[4], Ai Ing Lim[5], Andrew S. Burns[6], Elena Fontana[7], Marita Bosticardo[1], Cristina Corsino[1], Angelina Angelova[2], Ottavia M. Delmonte[1], Heather Kenney[1], Deanna Riley[8], Grace Smith[8], Lisa Ott de Bruin[9], Vasileios Oikonomou[1], Lucas Dos Santos Dias[1], Danielle Fink[10], Eric Bohrnsen[4], Cole D. Kimzey[4], Gian Luigi Marseglia[11,12], Guisela Alva-Lozada[13], Jenna R.E. Bergerson[1], Ana Brett[14,15], Karlla W. Brigatti[16], Dimana Dimitrova[17], Cullen M. Dutmer[18], Alexandra F. Freeman[1], Hanadys Ale[19], Steven M. Holland[1], Francesco Licciardi[20], Srdjan Pasic[21], Laura E. Poskitt[16], David E. Potts[22], Joseph F. Dasso[22], Svetlana O. Sharapova[23], Kevin A. Strauss[16], Brant R. Ward[24], Melis Yilmaz[22], Douglas B. Kuhns[10], Michail S. Lionakis[1], Stephen R. Daley[25], Heidi H. Kong[26], Julia A. Segre[27], Anna Villa[28,29], Stefania Pittaluga[8], Jolan E. Walter[22], Ivan Vujkovic-Cvijin[30], Yasmine Belkaid[5,31], and Luigi D. Notarangelo[1]

Partial RAG deficiency (pRD) can manifest with systemic and tissue-specific immune dysregulation, with inflammatory bowel disease (IBD) in 15% of the patients. We aimed at identifying the immunopathological and microbial signatures associated with IBD in patients with pRD and in a mouse model of pRD (*Rag1*$^{w/w}$) with spontaneous development of colitis. pRD patients with IBD and *Rag1*$^{w/w}$ mice showed a systemic and colonic Th1/Th17 inflammatory signature. Restriction of fecal microbial diversity, abundance of pathogenic bacteria, and depletion of microbial species producing short-chain fatty acid were observed, which were associated with impaired induction of lamina propria peripheral Treg cells in *Rag1*$^{w/w}$ mice. The use of vedolizumab in *Rag1*$^{w/w}$ mice and of ustekinumab in a pRD patient were ineffective. Antibiotics ameliorated gut inflammation in *Rag1*$^{w/w}$ mice, but only bone marrow transplantation (BMT) rescued the immunopathological and microbial signatures. Our findings shed new light in the pathophysiology of gut inflammation in pRD and establish a curative role for BMT to resolve the disease phenotype.

[1]Laboratory of Clinical Immunology and Microbiology, National Institute of Allergy and Infectious Diseases, National Institutes of Health, Bethesda, MD, USA; [2]Bioinformatics and Computational Biosciences Branch, Office of Cyber Infrastructure and Computational Biology, National Institute of Allergy and Infectious Diseases, National Institutes of Health, Bethesda, MD, USA; [3]Integrated Data Sciences Section, Research Technologies Branch, National Institute of Allergy and Infectious Diseases, National Institutes of Health, Bethesda, MD, USA; [4]Research Technologies Branch, Rocky Mountain Laboratories, National Institute of Allergy and Infectious Diseases, National Institutes of Health, Hamilton, MT, USA; [5]Metaorganism Immunity Section, Laboratory of Host Immunity and Microbiome, National Institute of Allergy and Infectious Diseases, National Institutes of Health, Bethesda, MD, USA; [6]NIAID Microbiome Program, National Institute of Allergy and Infectious Diseases, National Institutes of Health, Bethesda, MD, USA; [7]IRCCS Humanitas Research Hospital, Milan, Italy; [8]Laboratory of Pathology, National Cancer Institute, National Institutes of Health, Bethesda, MD, USA; [9]Willem-Alexander Children's Hospital, Department of Pediatrics, Pediatric Stem Cell Transplantation Program, Leiden University Medical Center, Leiden, Netherlands; [10]Neutrophil Monitoring Lab, Leidos Biomedical Research, Inc., Frederick National Laboratory for Cancer Research, Frederick, MD, USA; [11]Pediatric Unit, Department of Clinical, Surgical, Diagnostic, and Pediatric Sciences, University of Pavia, Pavia, Italy; [12]Pediatric Clinic, Fondazione IRCCS Policlinico San Matteo, Pavia, Italy; [13]Allergy and Immunology Division Hospital Nacional Edgardo Rebagliati Martins, Lima, Peru; [14]Hospital Pediátrico, Unidade Local de Saúde de Coimbra, Coimbra, Portugal; [15]Clínica Universitária de Pediatria, Faculdade de Medicina, Universidade de Coimbra, Coimbra, Portugal; [16]Clinic for Special Children, Gordonville, PA, USA; [17]Experimental Transplantation and Immunotherapy Branch, National Cancer Institute of the National Institutes of Health, Bethesda, MD, USA; [18]Allergy and Immunology, Children's Healthcare of Atlanta, Emory University School of Medicine, Atlanta, GA, USA; [19]Division of Immunology, Allergy and Rheumatology, Joe DiMaggio Children's Hospital, Memorial Healthcare System, Hollywood, FL, USA; [20]Immuno-reumatologia, Pediatria Specialistica Universitaria, Ospedale Infantile Regina Margherita, Torino, Italy; [21]Department of Pediatric Immunology, Mother and Child Health Institute, Medical Faculty, University of Belgrade, Belgrade, Serbia; [22]Division of Pediatric Allergy/Immunology, University of South Florida at Johns Hopkins All Children's Hospital, St. Petersburg, FL, USA; [23]Belarusian Research Center for Pediatric Oncology, Hematology and Immunology, Minsk, Belarus; [24]Division of Allergy and Immunology, Children's National Hospital, Washington, DC, USA; [25]Centre for Immunology and Infection Control, School of Biomedical Sciences, Faculty of Health, Queensland University of Technology, Brisbane, Australia; [26]Cutaneous Microbiome and Inflammation Section, National Institute of Arthritis and Musculoskeletal and Skin Diseases, National Institutes of Health, Bethesda, MD, USA; [27]Microbial Genomics Section, Translational and Functional Genomics Branch, National Human Genome Research Institute, National Institutes of Health, Bethesda, MD, USA; [28]San Raffaele-Telethon Institute for Gene Therapy (SR-Tiget), IRCSS San Raffaele Scientific Institute, Milan, Italy; [29]Milan Unit, Istituto di Ricerca Genetica e Biomedica, Consiglio Nazionale delle Ricerche, Milan, Italy; [30]Department of Biomedical Sciences, Cedars-Sinai Medical Center, Los Angeles, CA, USA; [31]Department of Immunology, Institut Pasteur, Paris, France.

**P. Subramanian and C. Oguz contributed equally to this paper. Correspondence to Luigi D. Notarangelo: luigi.notarangelo2@nih.gov; Francesca Pala: francesca.pala@nih.gov

*R. Castagnoli and F. Pala are co-first authors; R. Castagnoli's current affiliations are Pediatric Unit, Department of Clinical, Surgical, Diagnostic, and Pediatric Sciences, University of Pavia, Pavia, Italy and Pediatric Clinic, Fondazione IRCCS Policlinico San Matteo, Pavia, Italy. A.I. Lim's current affiliation is Department of Molecular Biology, Princeton University, Princeton, NJ, USA.

Introduction

The immune system shapes microbial composition and controls the maintenance of host–microbe symbiosis (Ansaldo et al., 2021). Likewise, the microbiota influences the development and function of the host's immunity (Hooper and Macpherson, 2010). This reciprocal relationship plays an important role in a variety of diseases with potential therapeutic implications (Gilbert et al., 2018). The gastrointestinal (GI) tract represents a unique interface environment to study interactions between the host's immune system and the microbiota (Fan and Pedersen, 2021; Rook et al., 2017). In particular, the surface expression of the T cell receptor (TCR) endows T cells with the capacity to mediate specific microbial recognition in the context of both mutualistic coevolution and pathology (Ivanov et al., 2022). The characteristics of a successful T cell response to a given microbe (whether pathogenic or commensal) are antigen specificity and appropriate functional differentiation into T helper (Th), T effector (Teff), or T regulatory (Treg) cells. While pro-inflammatory T cell responses are mainly directed at clearing pathogens, Treg cells survey the ecosystem to modulate immune response, maintaining peripheral tolerance while dampening tissue inflammation (Ivanov et al., 2022). The induction of specific peripheral Treg (pTreg) populations has been shown to be driven by microbial-derived metabolites, essential to establish a tolerogenic environment in the GI tract (Takeuchi et al., 2024).

The *RAG1* and *RAG2* genes encode for lymphoid-specific proteins that initiate the process of V(D)J recombination, allowing the assembly of variable (V), diversity (D), and joining (J) genes at the TCR and immunoglobulin loci (Fugmann et al., 2000). While functionally null (or quasi-null) variants in the *RAG* genes result in severe combined immunodeficiency with the absence of T and B lymphocytes ($T^-B^-NK^+$ SCID) (Schwarz et al., 1996) or Omenn syndrome (OS) (Villa et al., 1998), hypomorphic variants allowing for residual protein expression and function are responsible for various clinical phenotypes, globally defined as partial RAG deficiency (pRD) (Csomos et al., 2022) and characterized by partial development of T and B cells with a restricted repertoire.

Inflammatory bowel disease (IBD)–like colitis has been reported in up to 15% of pRD patients, being the most frequent manifestation of immune dysregulation in this condition, after autoimmune cytopenias (Delmonte et al., 2020). Here, to better characterize the pathophysiology of IBD associated with pRD, we studied a cohort of sixteen pRD patients, evaluated their clinical and immunological features, analyzed inflammatory signatures both in peripheral blood and in the colonic tissue, and characterized fecal microbiota composition. Moreover, we applied a multiomics strategy (including lamina propria [LP] $CD4^+$ T cell single-cell RNA-sequencing [scRNA-seq] and TCR repertoire analysis, and fecal microbiome and metabolome analysis), to study a mouse model of hypomorphic Rag1 deficiency ($Rag1^{R972W/R972W}$, from now on referred to as $Rag1^{w/w}$ mice) that presents with spontaneous development of colitis. This mouse model recapitulates the immunological phenotype seen in pRD patients, with a low number of naïve T cells, and a variable number of activated/memory T cells with a restricted TCR repertoire (Ott de Bruin et al., 2018). We show that $Rag1^{w/w}$ mice have an inflammatory Th1/Th17 signature already present at weaning, associated with abundance of T cells expressing the gut-homing α4β7 integrin in mesenteric lymph nodes (MLN). This inflammatory signature is accompanied by a reduction in microbiota diversity, with depletion of microbial species producing short-chain fatty acid (SCFA) both in pRD patients and in $Rag1^{w/w}$ mice, and defective induction of pTreg cells in the LP of $Rag1^{w/w}$ mice. We evaluated the capacity of various treatment modalities to correct intestinal and systemic inflammation. The use of antibiotics improved intestinal inflammation in $Rag1^{w/w}$ mice, but did not correct the Th1/Th17 skewing. The use of vedolizumab (targeting α4β7 integrin) in $Rag1^{w/w}$ mice and of ustekinumab (targeting IFN-γ and IL-17 production) in a pRD patient with IBD were ineffective in correcting intestinal inflammation. In contrast, both systemic and intestinal inflammatory signatures were corrected upon bone marrow transplantation (BMT), suggesting that this therapeutic approach might be beneficial in restoring complex interactions between the immune system and microbiota in pRD and potentially also in patients affected by other severe monogenic forms of immune dysregulation.

Results

Patients carrying biallelic hypomorphic *RAG* variants present with variable degrees of T and B cell lymphopenia and systemic inflammation and may develop chronic colitis

We studied a cohort of 16 pRD patients carrying biallelic *RAG* variants. All patients (11 males and 5 females, mean age 18.1 years, age range 16 mo–44 years) presented with a pRD phenotype showing a combination of severe and recurrent infections and clinical manifestations of immune dysregulation. Patients' demographics, genotype, clinical phenotype, and treatments for immune dysregulation are reported in Table 1. One third of the patients (P1–P5, 4 males and 1 female, mean age 11.9 years, age range 16 mo–37 years) presented with IBD-like colitis with protracted diarrhea and weight loss.

The patients exhibited variable degrees of T and B cell lymphopenia, associated with a significant reduction in the proportion of naïve T cells, while normal serum immunoglobulin A (IgA) and IgM levels were present in most of the patients (Fig. 1 A). Increased levels of CXCL9, IFN-γ, CXCL10, IL-17A, IL-10, and IL-6 were detected in the plasma of pRD patients irrespective of the IBD status (Fig. 1 B), consistent with the systemic inflammatory signatures recently described by our group in patients carrying *RAG* mutations (Bosticardo et al., 2025). Moreover, no statistically significant difference was observed in the residual recombination activity of *RAG* variants among pRD patients with or without IBD (Fig. S1 A).

Hematoxylin–eosin (H&E) staining of colonic samples of pRD patients with IBD showed active chronic colitis with mucosal architectural distortion, and immunohistochemistry and in situ

Table 1. **Demographic, molecular, and clinical features of pRD patients**

Patient #	Sex	Age at the time of the study	Gene defect	Allele 1; Allele 2	Infections	Immune dysregulation	Other complications	Treatment of immune dysregulation	BMT and outcome
P1	F	37 years	*RAG1*	p.C176F; p.C176F	Norovirus, URTI, LRTI, *Pseudomonas* pneumonia, bronchiectasis, *Salmonella* gastroenteritis, PJP	IBD, hypothyroidism	Hepatomegaly with bridging fibrosis and steatosis	Steroids	Yes, deceased
P2	M	16 mo	*RAG1*	p.A444V; p.V869F	URTI, LRTI, Aspergillus pneumonia, *Stenotrophomonas maltophilia*, *Citrobacter freundii*, adenovirus and norovirus gastroenteritis, *Helicobacter pylori*	VEOIBD, AIHA	Exocrine pancreatic insufficiency, cholestatic hepatitis	Steroids	Yes, A&W after 1 year
P3	M	8 years	*RAG1*	p.R112H; p.R112H	RTI	IBD		Ustekinumab	No, alive with IBD
P4	M	25 mo	*RAG1*	p.C176F; p.C176F	Recurrent bacterial and viral URTI, severe CMV viremia	VEOIBD with hematochezia and hematemesis		Tacrolimus	Yes, deceased
P5	M	11 years	*RAG1*	p.P152L; p.R973C	RTI, bronchiectasis	IBD, Evans syndrome		Steroids	Yes, A&W after 1 year
P6	M	32 years	*RAG2*	p.G451A; p.G451A	COVID-19, CMV, rubella		Liver fibrosis		No, deceased
P7	F	44 years	*RAG1*	p.R474C; p.R474C	Genital HPV and HSV, URTI, LRTI, bronchiectasis, *Pseudomonas*, pneumonia, MAC, Nocardia lung infection	Panarteritis nodosa, T1DM, hypothyroidism, pernicious anemia, arthritis, granulomas	Granulosa cell ovarian cancer	Etanercept, methotrexate	Yes, deceased
P8	F	6 years	*RAG1*	p.R112H; p.C328Y	Recurrent pneumonia, bronchiectasis, diarrhea	AIHA		Steroids	Yes, A&W after 5 years
P9	F	35 years	*RAG1*	p.W522C; p.R975Q	Recurrent HSV, URTI, LRTI, bronchiectasis, onychomycosis	Alopecia, vitiligo, arthritis, asthma	Ovarian insufficiency	Hydroxychloroquine	Yes, A&W after 3 years
P10	M	12 years	*RAG1*	p.Y562C; p.R841Q	URTI, LRTI, bronchiectasis, mastoiditis	AIHA, hypothyroidism, splenomegaly		Steroids	Yes, deceased
P11	M	3 years	*RAG1*	p.K86Vfs*33; p.C328Y	EBV viremia			Rituximab	Yes, deceased
P12	M	23 years	*RAG1*	p.R410W; p.R507Q	Warts, EBV viremia, URTI, LRTI	Vitiligo, alopecia, granulomas		Etanercept, adalimumab, hydroxychloroquine	Yes, A&W after 5 years
P13	M	39 years	*RAG1*	p.R108*; p.W522C	Warts, orolabial HSV, LRTI, bronchiectasis, MRSA, oral candidiasis	Alopecia, hypothyroidism, hypogonadism, granulomas		Steroids, MMF, rituximab	Yes, A&W after 6 years
P14	M	7 years	*RAG1*	p.G393V; p.G709A	URTI, LRTI, perianal abscess	Autoimmune hypothyroidism			Yes, A&W after 2 years
P15	F	12 years	*RAG1*	p.R404W; p.H747P	Herpes labialis, HSV keratitis, LRTI, septic shock, ecthyma gangrenosum	AIHA		MMF, rituximab, sirolimus	Yes, A&W after 5 years
P16	M	18 years	*RAG1*	p.K86Vfs*33; p.H612R	Chronic sinusitis, recurrent LRTI, bronchiectasis, COVID-19	AIHA, thyroiditis, vitiligo		Steroids	Yes, A&W after 21 mo

AIHA, autoimmune hemolytic anemia; A&W, alive and well; CMV, cytomegalovirus; EBV, Epstein-Barr virus; HPV, human papillomavirus; HSV, herpes simplex virus; IBD, inflammatory bowel disease; LRTI, lower respiratory tract infections; MAC, *Mycobacterium avium* complex; MMF, mycophenolate mofetil; MRSA, methicillin-resistant *Staphylococcus aureus*; PJP, *Pneumocystis jirovecii* pneumonia; RTI, respiratory tract infections; T1DM, type 1 diabetes mellitus; URTI, upper respiratory tract infections; VEOIBD, very early-onset inflammatory bowel disease.

hybridization revealed prominent CD3⁺ T cell infiltrates and increased levels of *IFNG* and *CXCL9* transcripts, respectively (Fig. 1 C and Fig. S1 B). Together, these data demonstrate that pRD is characterized by systemic and tissue-specific inflammatory signatures with up-regulation of IFN-γ signaling and skewing toward Th1/Th17 immune responses. Based on these findings, we aimed at further dissecting the pathogenesis of chronic colitis in *Rag1*$^{w/w}$ mice.

Rag1$^{w/w}$ mice spontaneously develop colitis with LP T cell infiltrates and systemic inflammation that worsens with age

We have previously demonstrated that *Rag1*$^{w/w}$ mice have impaired generation of T and B cells in the thymus and bone marrow, resulting in peripheral lymphopenia, with markedly reduced proportion of naïve T cells and increased percentage of activated/memory T cells, restricted TCR repertoire, hypogammaglobulinemia, impaired specific antibody production, and signs of immune dysregulation, as indicated by elevated serum IgE and production of a broad range of autoantibodies (Ott de Bruin et al., 2018). These features recapitulate the immunological phenotype seen in pRD patients.

Analysis of intestinal pathology in *Rag1*$^{w/w}$ mice revealed spontaneous colitis, macroscopically characterized by substantial thickening of the colon throughout its entire length. H&E staining of colonic samples from 10- to 12-wk-old *Rag1*$^{w/w}$ mice showed colonic architectural disruption with epithelial hyperplasia, crypt elongation, and prominent inflammatory cell infiltrate consisting mainly of CD3⁺ T cells in the colon LP (Fig. 2 A). To quantify the histologic abnormalities, we used a colitis score that evaluates the degree of architectural disruption, inflammatory infiltrate, and muciparous gland activity, ranging from zero (normal) to 10, corresponding to the most severe alterations (Rigoni et al., 2016). Comparing the colitis score of male and female mice at 12 wk of age, we observed that colitis was more severe in female mice (Fig. S2 A). For this reason, further studies were focused on female *Rag1*$^{w/w}$ mice. We observed that the colitis score of female *Rag1*$^{w/w}$ mice increases over time as mice age, with the histologic changes becoming evident only after weaning (Fig. 2 B).

The increased expression of *Ifng* and *Cxcl9* transcripts was detected by in situ hybridization in *Rag1*$^{w/w}$ colonic specimens at 10–12 wk of age (Fig. 2 C), similar to what observed in pRD patients with IBD. In addition, real-time quantitative polymerase chain reaction (qPCR) analysis showed higher levels of *Ifng* and *Il17* transcripts in the colonic tissue from *Rag1*$^{w/w}$ mice (Fig. S2 B). Besides an increased frequency of activated, pro-inflammatory CD4⁺ T cells, also the frequency of myeloid cells (especially neutrophils and monocytes) was increased in the LP of *Rag1*$^{w/w}$ mice (Fig. S2, C and D).

Since the colonic inflammation was associated with prominent T cell infiltrates, we aimed at studying the T cell phenotype in locally draining MLN. A higher proportion of activated Teff cells (identified as CD44^{high}CD62L^{low} CD3⁺ T cells) was observed in MLN from 12-wk-old *Rag1*$^{w/w}$ mice (Fig. S2 E). In addition, a significantly higher percentage of MLN T cells expressed the integrin α4β7 (Fig. S2 F), which is responsible for T cell homing into gut-associated lymphoid tissues through its binding to the mucosal addressin cell adhesion molecule (Kurmaeva et al., 2014). Finally, to assess systemic inflammation, we measured serum levels of several cytokines, and demonstrated a progressive increase over time in IFN-γ, CXCL9, CXCL10, IL-2, TNF-α, IL-12p70, and IL-17A/F levels in *Rag1*$^{w/w}$ mice (Fig. S2 G), mirroring what was observed in pRD patients.

Colonic LP CD4⁺ T cells of *Rag1*$^{w/w}$ mice show a Th1/Th17 inflammatory signature associated with a restricted TCR repertoire

Based on these findings, we focused on characterizing the colonic inflammation in *Rag1*$^{w/w}$ mice. Flow cytometry analysis of LP immune cells at different ages revealed that the T lymphocytic infiltrate, determined as TCRβ⁺ cells, is quantitatively similar in *Rag1*$^{w/w}$ and wild-type mice at 3 wk of age, but is significantly increased at 12 wk of age in *Rag1*$^{w/w}$ mice (Fig. 2 D), paralleling the worsening of the colitis score. Flow cytometry analysis of LP Th lymphocytes (identified as TCRβ⁺, CD4⁺, Foxp3⁻ cells) demonstrated that *Rag1*$^{w/w}$ mice have an increased percentage of CD4⁺ T cells expressing IFN-γ and/or IL-17 compared with wild-type controls (Fig. 2, E and F). Noteworthily, an increased proportion of IFN-γ⁺/IL-17⁺ double-positive T cells, frequently identified in the inflamed LP of patients and murine models of IBD (Annunziato et al., 2007), were observed in *Rag1*$^{w/w}$ mice. This T cell phenotype was already present in *Rag1*$^{w/w}$ mice at 3 wk of age (Fig. 2, E and F), even before development of a significant T cell infiltrate (Fig. 2 G), suggesting that the Th1/Th17 skewing of *Rag1*$^{w/w}$ mouse CD4⁺ T cells is genetically determined.

To further study the T cell–mediated immune dysregulation, we performed scRNA-seq of sorted LP CD4⁺ T from *Rag1*$^{w/w}$ mice and wild-type controls at 3 and 12 wk of age. Differential gene expression identified 11 transcriptionally distinct CD4⁺ T cell subsets (Fig. S3 A). Based on the differential gene expression and known markers from the literature, we were able to annotate these different subsets (Fig. S3 B). In particular, Tregs were the more abundant population and were identified by the expression of *Foxp3*; naïve CD4⁺ T cells expressed high levels of *Ccr7* and *Sell*, while activated T cells were positive for *Nkg7*. We identified T follicular helper (Tfh) cells expressing *Tcf7* and *Cxcr5*, and a small population of Th2 cells expressing the *Il4* gene. Several populations expressing high levels of *Il17*, *Ifng*, and interferon-responsive genes were identified, similar to what was seen by flow cytometry. When we looked at the different sample contribution to these subsets, an enrichment in CD4⁺ T cells expressing the *Ifng* and *Il17* transcripts was present in *Rag1*$^{w/w}$ mice already at 3 wk of age, along with a marked reduction in the proportion of naïve CD4⁺ T cells (Fig. 3, A and B). Flow cytometry demonstrated that FOXP3⁺ T cells represented ∼20% of total LP CD4⁺ cells in both wild-type and *Rag1*$^{w/w}$ mice; however, due to the increased abundance of total TCRβ⁺ cells, the absolute count of FOXP3⁺ cells was significantly increased in *Rag1*$^{w/w}$ mice (Fig. S3 C).

To better define transcriptional signatures characteristic of T cell subtypes, we performed gene set enrichment analysis comparing the LP CD4⁺ T cell expression profiles in *Rag1*$^{w/w}$ mice and wild-type controls at 12 wk of age. Pathways enriched in

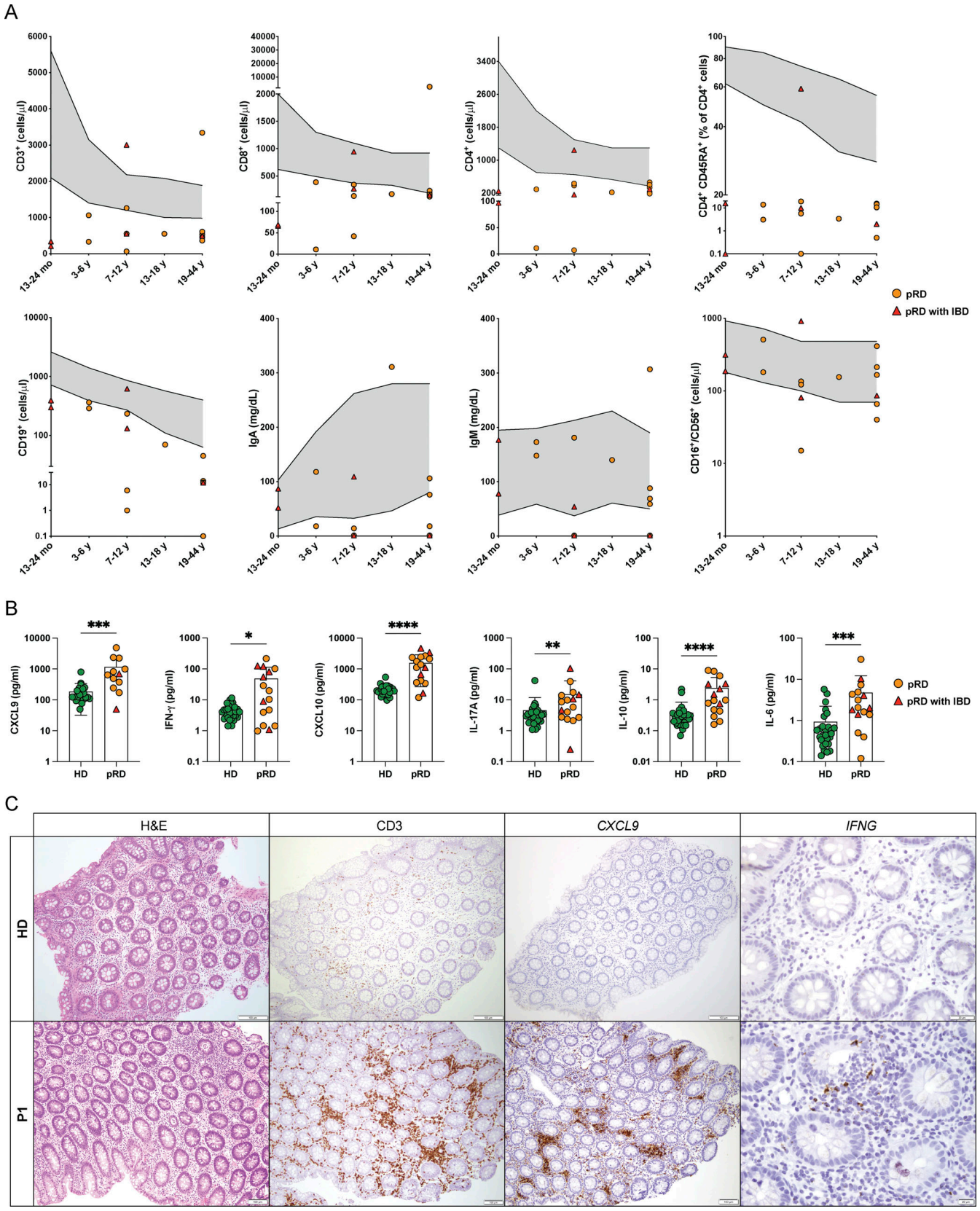

Figure 1. **Patients with pRD present with architectural distortion and T cell infiltrates in colonic tissue. (A)** Scatter plots showing CD3⁺ cell counts, CD8⁺ cell counts, CD4⁺ cell counts, frequency of CD45RA⁺ CD4⁺ cells, CD19⁺ cell counts, IgA and IgM concentration, and CD16⁺/CD56⁺ cell counts in peripheral blood of patients at the time of analysis. Each pRD patient is identified with an orange dot, and red triangles indicate patients with IBD. The gray area inside each graph shows the range of values for HD individuals. **(B)** Bar plots (mean with SD) showing serum cytokine levels in HD (n = 32) and patients with pRD

(*n* = 13). Red triangles indicate pRD subjects with IBD. Statistical analysis was performed using a Mann–Whitney test. **(C)** Immunohistochemical and RNAscope analyses of colon biopsy isolated from one HD and one pRD patient (P1), showing H&E and CD3 staining, as well as expression of *CXCL9* and *IFNG* transcripts. All images are 10× magnification (scale bars: 100 µm), while *IFNG* is 40× magnification (scale bar: 20 µm). *P < 0.05, **P < 0.01, ***P < 0.001, ****P < 0.0001. y, years.

IFN-γ response and Tfh subsets of *Rag1*$^{w/w}$ mice included "T cell activation," "response to interferon-gamma," "response to interferon-alpha," "response to chemokine" and "regulation of leukocyte activation" (Fig. 3 C). Furthermore, pathway analysis demonstrated enrichment in "negative regulation of immune system process" and "negative regulation of cell activation" in the IFN-γ$^+$ and IL-17$^+$ clusters of LP CD4$^+$ T cells in wild-type compared with *Rag1*$^{w/w}$ mice (Fig. S3 D). These data are consistent with active LP inflammatory processes associated with chronic colitis in *Rag1*$^{w/w}$ mice. Finally, inflammatory signatures of cell activation in *Rag1*$^{w/w}$ mice were more prominent at 12 wk of age than at 3 wk of age (Fig. S3 E).

On the same samples, we also performed single-cell TCR sequencing with the goal of defining the TCR repertoire of LP CD4$^+$ T cells. A severe restriction of the TCR-β (TRB) repertoire of sorted LP CD4$^+$ T cells was observed in *Rag1*$^{w/w}$ mice, with nearly 20% of hyperexpanded clonotypes (abundance >100 per clonotype, each of which is defined by a unique TCR-α [TRA]-TRB pairing) already present at 3 wk of age (Fig. 3 D). Hyperexpanded clonotypes were observed especially among CD4$^+$ T cells expressing *Ifng* and among cells in the IFN-γ response cluster (Fig. 3 E). Analysis of the amino acid composition of the complementarity-determining region 3 (CDR3) of TRB clonotypes in LP CD4$^+$ T cells of *Rag1*$^{w/w}$ mice revealed increased abundance of hydrophobic amino acids (Fig. 3 F), known molecular biomarkers of self-reactive T cells (Stadinski et al., 2016).

Overall, these data indicate that the colitis observed in *Rag1*$^{w/w}$ mice is characterized by a CD4$^+$ T cell infiltrate in the LP with an immunological phenotype and transcriptional profile consistent with Th1/Th17 inflammatory signatures, T cell activation, and expansion of T cell clonotypes with characteristics of self-reactivity. This phenotype is already present early in life, whereas the colonic inflammation histologically manifests only after weaning, a time of profound remodeling (and reactivity) of the host–microbiota relationship (Lubin et al., 2023), suggesting a potential role of altered interactions between the host's immune system and the microbiota in driving and sustaining colonic inflammation.

The fecal microbiota of pRD patients and *Rag1*$^{w/w}$ mice is characterized by a severe restriction of microbial diversity with specific microbial signatures

To characterize the composition of intestinal microbiota in pRD patients, we performed 16S rRNA gene sequencing analysis on fecal samples from 15 pRD patients (P1, P3-P16) and 23 healthy controls (HC). Firstly, pRD patients, independently from the presence of IBD, showed a significant reduction of fecal microbiota alpha diversity (Fig. 4 A), a signature commonly associated with several pathological conditions including IBD (Ott et al., 2004). This reduced gut microbiota diversity in IBD is especially manifested in a loss of gut bacteria capable of producing SCFA, microbial metabolites that dampen inflammation (Arpaia et al., 2013; Smith et al., 2013) and bolster gut barrier integrity (Wang et al., 2020). The loss of these taxa is thought to contribute to IBD progression, though the dynamics of these metabolites and the taxa that produce them in pRD remains poorly understood.

To understand whether reduced alpha diversity in pRD was associated with altered microbiota composition, we studied the differential abundance of microbial species in pRD patients and HC. A significant increase in the relative abundance of oral bacteria, including the *Streptococcus* genus, was detected in the gut microbiota of pRD patients (Fig. 4 B and Fig. S4 A). In this context, there is increasing evidence that microorganisms of the oral cavity, ectopic to the gut, may trigger intestinal inflammation (Atarashi et al., 2017; Kitamoto et al., 2020; Read et al., 2021). Further analysis of microbial differential abundance between pRD and HC identified a significant reduction in the relative abundance of the *Ruminococcaceae* family, which contains numerous SCFA producers (Fig. 4 C), and, at the genus level, a significant reduction of SCFA producers *Butyricicoccus* and *Coprococcus* (Fig. 4 D) in pRD patients.

Gut mucosal IgA is a host molecule that promotes host–microbe symbiosis by binding gut bacteria and tethering them to host mucus to prevent their penetration into host tissues (Pabst and Slack, 2020; Yang and Palm, 2020). This tethering can additionally enhance colonization of targeted bacteria (Donaldson et al., 2018). To assess whether reduced abundance of taxa in pRD patients was associated with diminished IgA against the same taxa, we performed IgA-sequencing (IgA-seq) profiling on pRD patients and HC.

Firstly, when examining the total antimicrobial mucosal IgA repertoire, pRD and HC tended to cluster separately (Fig. 4 E). Moreover, concomitant with diminished relative abundance of *Ruminococcaceae* and *Coprococcus* observed in pRD patients, we found that *Coprococcus* was less IgA-coated in pRD patients as compared to HC, as was the prominent SCFA-producing genus *Faecalibacterium* (Fig. 4 F).

To evaluate whether similar microbial signatures were observed also in the mouse model, we performed 16S rRNA gene sequencing on murine fecal samples collected from *Rag1*$^{w/w}$ mice and wild-type controls. Firstly, we analyzed the fecal microbiota from co-housed *Rag1*$^{w/w}$ and wild-type mice. Co-housing represents a standard approach in mouse facilities, and it is known to normalize the microbiota composition of mice kept in the same cage. Analysis of the fecal microbiota in co-housed 12-wk-old *Rag1*$^{w/w}$ and wild-type mice revealed a significant reduction of microbiota alpha diversity in *Rag1*$^{w/w}$ mice (Fig. 4 G). The observation that *Rag1*$^{w/w}$ mice manifested a low alpha diversity in their microbiota, even when co-housed with wild-type mice, indicates a very strong effect of genotype on microbial

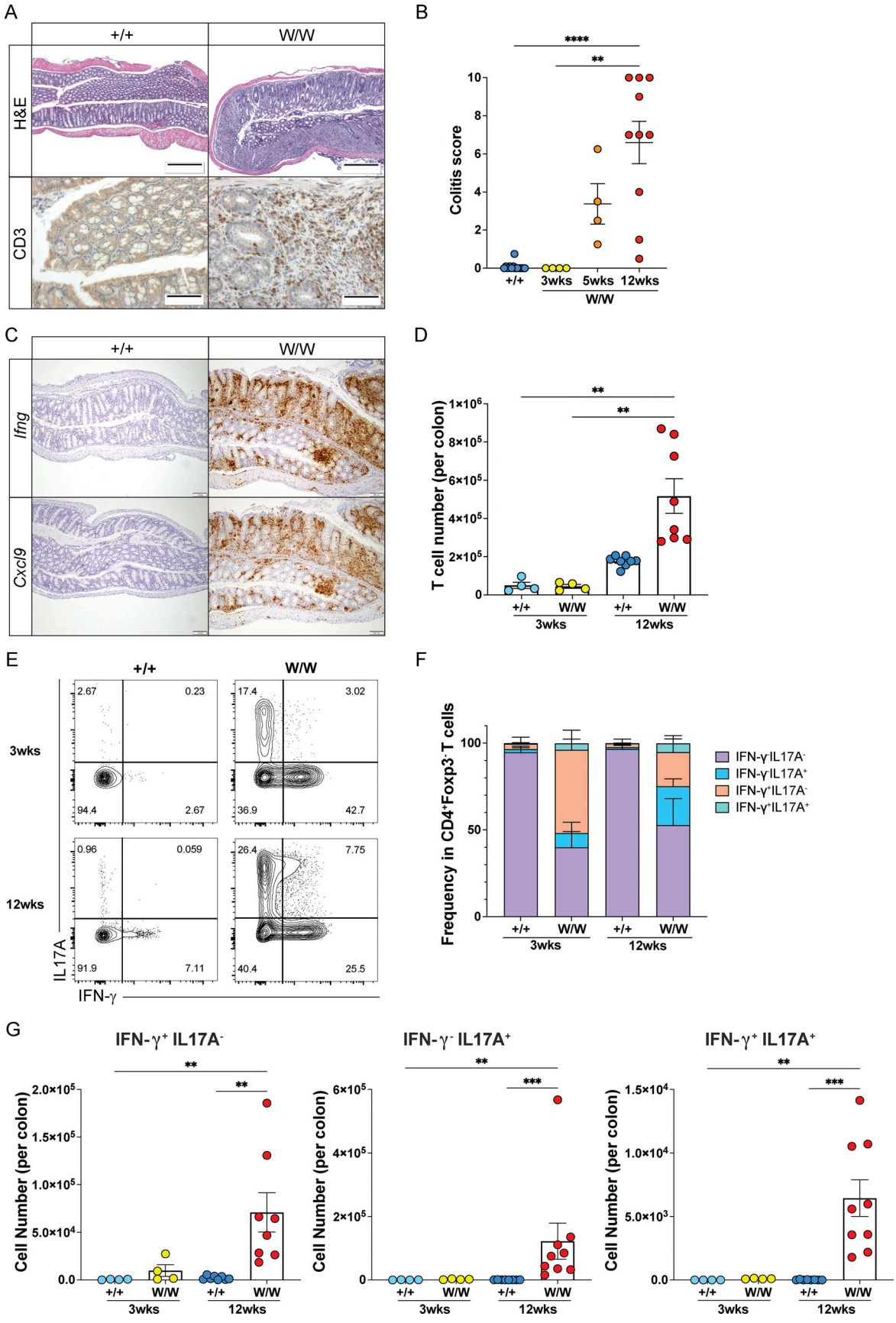

Figure 2. **Hypomorphic *Rag1*$^{R972W/R972W}$ (W/W) mutant mouse model recapitulates the human phenotype with architectural distortion and T cell infiltrates in colonic tissue. (A)** Immunohistochemical analysis of colon biopsy isolated from a wild-type (+/+) and a *Rag1*$^{w/w}$ (W/W) mouse at 12 wk of age

showing H&E staining (4× magnification, scale bar: 500 µm) and CD3 staining (20× magnification, scale bar: 100 µm). **(B)** Colitis score based on immunohistochemical analysis of 12-wk-old +/+ littermate mice (n = 13), and 3-wk-old (n = 4), 5-wk-old (n = 4), and 12-wk-old W/W mice (n = 10). Bars show the mean with SEM. **(C)** RNAscope analysis of the colon biopsy from a wild-type and a *Rag1*$^{w/w}$ mouse at 12 wk of age, showing the expression of *Ifng* and *Cxcl9* transcripts (10× magnification, scale bar: 100 µm). **(D)** Bar plot shows absolute counts of total TCRβ$^+$ T cells isolated from the LP of 3-wk-old littermate +/+ and W/W mice (n = 4/group), and 12-wk-old littermate +/+ and W/W mice (n = 8/group). Bars show the mean with SEM. **(E and F)** (E) Representative contour plots of cytokine production by Th cells after restimulation and subset distribution (F) of CD4$^+$ T cells isolated from the LP of littermate +/+ and W/W mice at 3 and 12 wk of age. **(G)** Total cell number of colonic LP IL-17A– and IFN-γ–producing Th cells. In E–G, all flow plots were gated on live CD45$^+$CD90.2$^+$TCRβ$^+$CD4$^+$Foxp3$^-$ cells. Data are from at least three independent experiments. Groups were compared using a Kruskal–Wallis test with Dunn's multiple comparisons correction (B, D, and G). **P < 0.01, ***P < 0.001, ****P < 0.0001.

composition. In order to assess whether worsening of colonic inflammation over time correlates with changes in microbiota composition, we performed a longitudinal time course analysis on fecal samples collected from *Rag1*$^{w/w}$ mice and wild-type controls at different time points (3, 5, 10, and 14 wk of age) and housed separately. Significantly reduced alpha diversity of the microbiota was observed in *Rag1*$^{w/w}$ mice, which became more evident particularly at 10 and 14 wk of age (Fig. 4 H). Beta diversity principal component analysis showed that *Rag1*$^{w/w}$ and wild-type mice cluster separately, with completely independent clustering at 14 wk of age (Fig. S4 B).

Further analysis of microbial differential abundance between *Rag1*$^{w/w}$ and wild-type mice identified a significant progressive reduction in the relative abundance of the *Ruminococcaceae* family in mutant mice (Fig. 4 I) as was seen in pRD patients, and, at the genus level, a significant reduction of *Intestinimonas*, *Lachnospiraceae*, and *Oscillibacter* that became more prominent over time (Fig. S4, C and D). Moreover, concordant with human data, IgA-seq profiles of *Rag1*$^{w/w}$ and wild-type mice cluster separately (Fig. 4 J); in addition, the *Ruminococcaceae* family was significantly less IgA-coated in mutant mice as compared to wild-type mice (Fig. 4 K).

The *Ruminococcaceae* family belongs to the Firmicutes phylum and is known to be enriched for SCFA-producing bacteria (Deleu et al., 2021; Fusco et al., 2023). To investigate for possible differences in the representation of metabolic pathways between *Rag1*$^{w/w}$ and wild-type mice, we utilized phylogenetic investigation of communities by reconstruction of unobserved states (PICRUSt) analysis. PICRUSt can predict microbial community function by inferring from marker gene sequencing using curated reference genome databases (Langille et al., 2013). Pathways related to SCFA production ("pyruvate fermentation to butanoate"; "acetyl-CoA fermentation to butanoate II"; "L lysine fermentation to acetate and butanoate") were significantly depleted in *Rag1*$^{w/w}$ mutant mice (Fig. 4 L). Subsequent fecal metabolomics assessment of *Rag1*$^{w/w}$ mice showed broad metabolic abnormalities, with decreased fecal SCFA levels in *Rag1*$^{w/w}$ mice (Fig. 4 M), in agreement with the altered microbiota landscape.

Depletion of fecal SCFA in *Rag1*$^{w/w}$ mice is associated with alteration in the effector pTreg compartment

SCFAs are known to play an important role in the generation of pTreg cells in the colon and in supporting their suppressive function (Smith et al., 2013). Therefore, we investigated whether the depletion of SCFA was associated with altered Treg composition in the colon LP CD4$^+$ cells of *Rag1*$^{w/w}$ mice. While Foxp3 is the master regulator of Treg development (Fontenot et al., 2003), Helios and Rorc have been used to identify thymic/central Treg (tTreg) and pTreg subpopulations, respectively, in the GI tract (Sefik et al., 2015; Thornton et al., 2010; Xu et al., 2018). In addition, a substantial proportion of Helios$^+$ GI Tregs also express Gata3 (Wohlfert et al., 2011) and the surface molecule Neuropilin-1 (Singh et al., 2015), whereas Rorc$^+$ Tregs largely co-express c-Maf and IL-10 (Xu et al., 2018). Single-cell RNA-seq data of sorted LP CD4$^+$ T cell showed no significant depletion on the Treg cluster in *Rag1*$^{w/w}$ mice (Fig. 3, A and B). To better characterize the transcriptomic profile and subset distribution of LP Treg, we performed a subcluster analysis of the Treg cluster and identified six subpopulations (Fig. 5 A). *Rorc* and *Il10* expression was detected in clusters 2 and 3, identifying these cells as effector pTreg. In contrast, clusters 0, 1, 4, and 5 were characterized by high levels of tTreg markers such as *Gata3* and *Ikzf2* (the latter encoding for Helios) (Fig. 5 B). When we investigated whether these clusters were equally represented in wild-type and *Rag1*$^{w/w}$ mice, we observed a marked depletion in microbiota-induced *Rorc*$^+$/*Maf*$^+$ *Il10*$^+$ pTreg, and enrichment of *Ikzf2*$^+$ *Gata3*$^+$ tTreg in *Rag1*$^{w/w}$ mice at 12 wk of age (Fig. 5 C). Moreover, flow cytometry analysis confirmed the reduction of RORγt$^+$ Treg cells in the LP of *Rag1*$^{w/w}$ mice at 12 wk of age (Fig. 5 D).

Together, these data indicate that the reduction of SCFA-producing microbial species that becomes evident after weaning in *Rag1*$^{w/w}$ mice is associated with a reduction in SCFA-dependent *Rorc*$^+$/*Maf*$^+$ *Il10*$^+$ effector pTreg cells, possibly altering mechanisms of immune homeostasis and promoting colonic inflammation. In line with recent data in wild-type mice (Gu et al., 2024), we found little co-expression of *Rorc* and *Gata3* also in *Rag1*$^{w/w}$ mice (1.99% and 1.31%, respectively) (Fig. 5 E). Finally, an increased representation of hyperexpanded clonotypes was detected in the *Ikzf2*$^+$ *Gata3*$^+$ tTreg compartment of *Rag1*$^{w/w}$ mice at 12 wk of age (Fig. 5 F).

Broad-spectrum antibiotics ameliorate gut inflammation in *Rag1*$^{w/w}$ mice, but only BMT rescues the immunological and microbial signatures

To assess the relative role of host and microbiota abnormalities in the pathogenesis of chronic colitis, we evaluated different treatments targeting either the microbiota or the immune cells in *Rag1*$^{w/w}$ mice. In particular, considering the higher percentage of MLN T cells expressing the gut-homing integrin α4β7 in *Rag1*$^{w/w}$ mice, we tested the effects of vedolizumab, a monoclonal antibody targeting the α4β7 integrin and currently approved in humans for the treatment of Crohn's disease and ulcerative

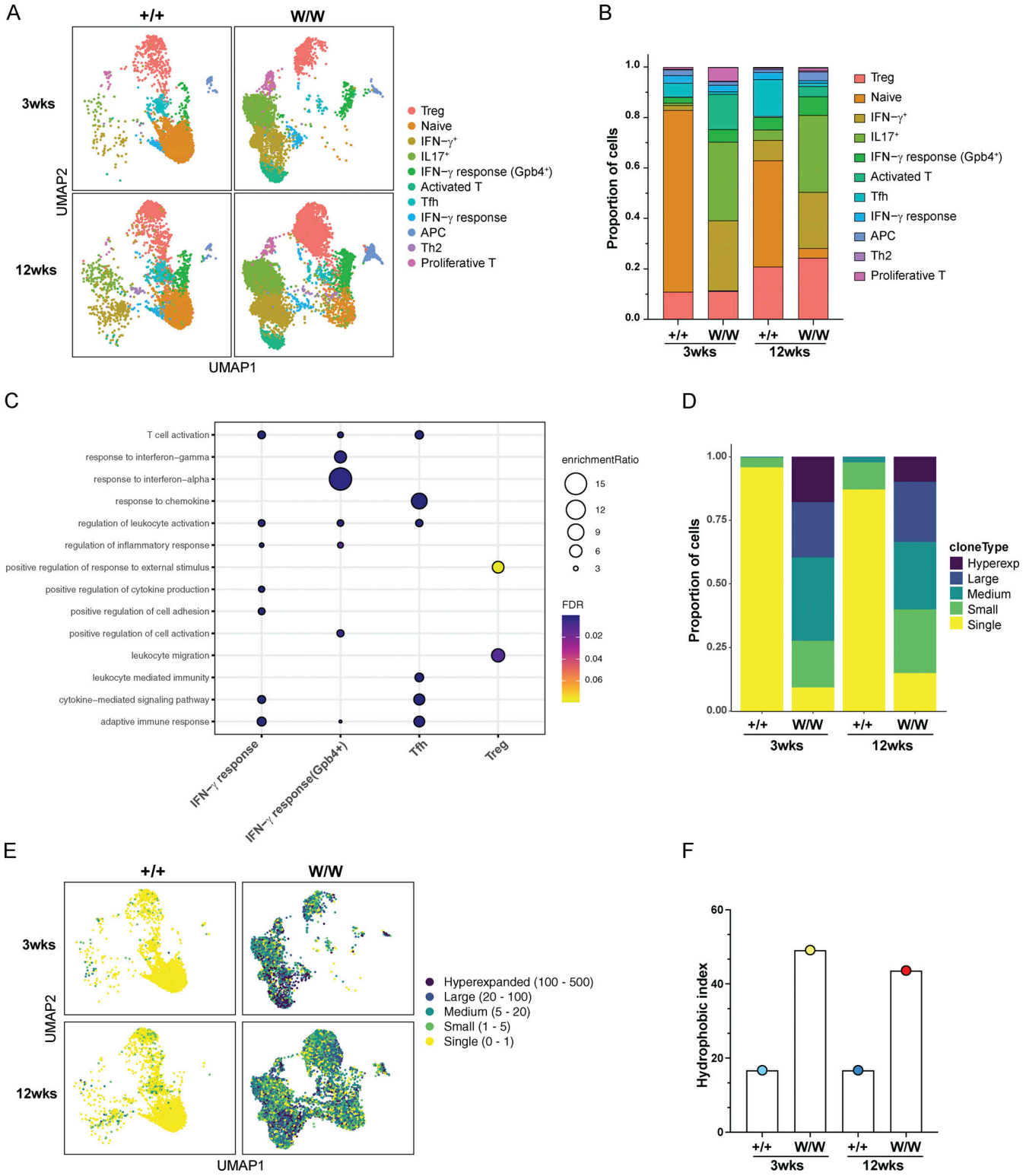

Figure 3. **Transcriptional profile of colonic LP CD4⁺ T cells confirms a Th1/Th17 signature and reveals restriction of TCR repertoire.** Total CD4⁺ T cells were sorted from the colonic LP of littermate wild-type (+/+) or *Rag1*$^{w/w}$ (W/W) mice at 3 and 12 wk of age, and analyzed by scRNA-seq. **(A)** UMAP plots showing the expression profiles of CD4⁺ T cells split by condition. Colors represent cells clustered together on the basis of similarity of global gene expression. **(B)** The stacked bar plot shows cluster distribution in each condition. **(C)** Selected gene ontology (GO) biological process terms enriched among gene sets differentially regulated (with >50% fold change and FDR = 0) in a cell type–specific manner between W/W and +/+ mice at 12 wk of age. The color of each circle represents the FDR value of the enriched GO term, whereas the size of each circle is proportional to the enrichment ratio, which is the number of differentially expressed genes associated with the GO term normalized by the number of such genes that one can encounter by random chance given the size of the total gene set in the GO database. **(D)** TCR clonotype analysis shows the proportion of different clonotype abundance ranges (single: 1 cell; small: 2–5 cells; medium:

6–20 cells; large: 21–100 cells; and hyperexpanded: 101–500 cells) of total CD4⁺ T cells sorted from the colonic LP of +/+ or W/W at 3 and 12 wk of age and analyzed by scRNA-seq. **(E)** TCR clonotype analysis projected on UMAP of CD4⁺ T cells split by condition. The color scale matches the abundance range as in D. **(F)** Hydrophobicity index of the CDR3 region of TRB clonotypes of LP CD4⁺ T cells from +/+ and W/W mice at 3 and 12 wk of gestational age. Single-cell samples were obtained from four to five pooled mice/group. Data are from two independent experiments.

colitis (Wyant et al., 2016). 10-wk-old *Rag1*$^{w/w}$ mice received 200 µg of vedolizumab or of isotype control every 2 days for 2 wk and then every 5 days until sacrifice after 45 days from treatment initiation (Fig. 6 A), following a protocol previously published (Lindebo Holm et al., 2012). Moreover, we tested the role of antibiotics in depleting gut microbial species and possibly dampening the microbiota-induced inflammation. To this purpose, we chose the broad-spectrum antibiotic cocktail with ampicillin, neomycin, metronidazole, and vancomycin (ANMV), as it has been widely used in murine studies to ablate microbiota (Sim et al., 2022). ANMV were administered with three different modalities (Fig. 6 B): (1) for 4 wk (8–12 wk of age), (2) starting at 3 wk of age, or (3) to pregnant mothers, to expose the mice to antibiotics since fetal life, and continuing ANMV until 12 wk of age in *Rag1*$^{w/w}$ offspring. Finally, another group of *Rag1*$^{w/w}$ mice received BMT at 7 wk of age after lethal total body irradiation (TBI), and were analyzed 20 wk after transplantation (Fig. 6 C). Treatment conditions were compared with wild-type mice and untreated *Rag1*$^{w/w}$ mice.

While vedolizumab proved ineffective in ameliorating colitis, broad-spectrum ANMV antibiotics (independently from the schedule of administration) and BMT significantly improved the colonic inflammation, with a marked reduction in the colitis score at histologic evaluation (Fig. 6 D), normalization of the LP T cell numbers by flow cytometry analysis (Fig. 6 E), and significant reduction of the *Cxcl9* and *Ifng* inflammatory signature (Fig. 6 F). However, both vedolizumab and ANMV-treated mice retained a high percentage of LP CD4⁺ T cells expressing IFN-γ and/or IL-17 (Fig. 6 G and Fig. S5 A). Moreover, scRNA-seq on sorted CD4⁺ T cells infiltrating the colon LP in ANMV-treated *Rag1*$^{w/w}$ mice showed persistence of cells expressing the *Ifng* and *Il17* transcripts (Fig. 6 H). The use of broad-spectrum antibiotics was associated with a redistribution of Treg subsets in ANMV-treated compared with untreated *Rag1*$^{w/w}$ mice (compare Fig. S5 B and Fig. 5 C). However, while the pattern of *Il10*-expressing Tregs mirrored what observed in wild-type mice, defective *Il10* expression was not rescued by ANMV treatment (Fig. S5 C).

Among *Ikzf2*⁺ *Rorc*⁻ *Il10*⁻ tTreg cells, analysis of TCR repertoire demonstrated a significant overlap of TRA clonotypes between ANMV-treated and untreated *Rag1*$^{w/w}$ mice at 12 wk (Fig. S5 D). We also observed that the LP tTreg repertoire of *Rag1*$^{w/w}$ mice was already established at 3 wk (as shown by clonotype overlap of *Ikzf2*⁺ *Rorc*⁻ *Il10*⁻ cells between 3-wk- and 12-wk-old mice). A similar effect (although less pronounced) was seen also in wild-type mice (Fig. S5 D). These data suggest that the shaping and the restriction of the TCR repertoire of tTreg cells in *Rag1*$^{w/w}$ mice are not driven by the microbiota, but are genetically established since early in life. Notably, no overlap was seen in the TRA repertoire of wild-type and *Rag1*$^{w/w}$ mice within either the tTreg or the pTreg compartments.

Among the various treatment modalities attempted, BMT was the only one that allowed resolution of the Th1/Th17 colonic inflammatory signature in *Rag1*$^{w/w}$ mice (Fig. 6 G). In addition, BMT was associated with a significant reduction in systemic inflammation, as shown by the normalization of IFN-γ, CXCL10, CXCL9, TNF-α, IL-2, and IL-10 plasma levels (Fig. 6, I and J; and Fig. S5 E). In contrast, ANMV treatment was only partially effective in dampening systemic inflammation, and minimal changes of plasma levels of inflammatory biomarkers were observed upon treatment with vedolizumab (Fig. 6, I and J; and Fig. S5 E).

BMT had also prominent effects on microbiota diversity and composition, as demonstrated by normalization of microbiota alpha diversity (Fig. 6 K) and increased relative abundance of *Intestinimonas*, *Lachnospiraceae*, and *Oscillibacter* genera (Fig. 6 L). Finally, analysis of fecal metabolome in BMT-treated *Rag1*$^{w/w}$ mouse composition showed an increase in SCFA levels compared with untreated *Rag1*$^{w/w}$ mice (Fig. 6 M).

We also investigated the effects of BMT and of ustekinumab (targeting IFN-γ and IL-17 production) in pRD patients. Among nine pRD patients who are alive after BMT, plasma levels of inflammatory biomarkers before and after definitive treatment were measured in seven of them, including two with IBD (P2 and P5 in Table 1). Plasma levels of IFN-γ, CXCL10, and IL-17A normalized after BMT (Fig. 7 A). Comparison of gut microbiota diversity and composition in two pRD patients (P8, P12) in which fecal samples were collected before and after BMT showed a trend toward normalization of alpha diversity (Fig. 7 B), and relative abundance of oral bacteria (Fig. 7 C) and of Firmicutes (Fig. 7 D). Four of the five patients with IBD (P1, P2, P4, and P5) received BMT. P1 and P4 died of respiratory failure and sepsis, and of disseminated cytomegalovirus infection, respectively, a few months after BMT. The two patients who survived (P2 and P5) had full resolution of GI symptoms after BMT; fecal calprotectin levels before and after BMT were measured in P2, documenting resolution of GI tract inflammation (1,549 µg/g before BMT versus 9 µg/g after BMT; normal value: <50 µg/g). In contrast, treatment with ustekinumab was ineffective to treat IBD in patient P3, in spite of an increase in the frequency of administration of this drug after 6 mo of treatment. After 9 mo of treatment with ustekinumab, P3 continued to have diarrhea and abdominal pain, and fecal calprotectin levels remained elevated (223 µg/g compared with 114 µg/g before treatment). A repeat colonic biopsy performed after 2 years of treatment with ustekinumab showed worsening of T cell infiltrates and persistence of inflammation (Fig. 7 E), prompting referral for BMT.

Discussion

In this study, we sought to identify disease-specific immunopathological and microbial changes driving severe and drug-resistant chronic colitis in pRD patients.

The spectrum of RAG deficiency phenotypes correlates with recombination activity of the mutant RAG alleles, with minimal

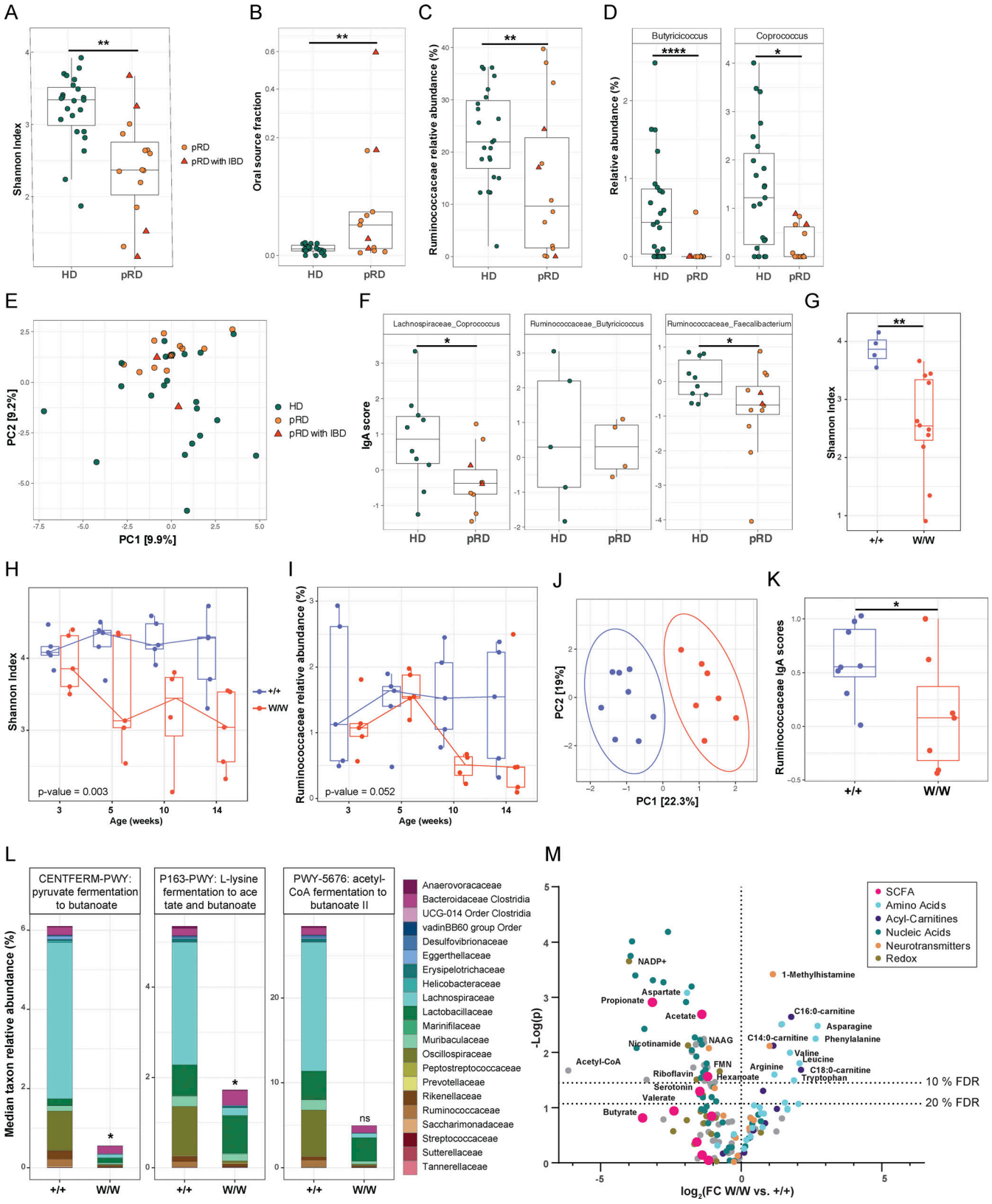

Figure 4. **Fecal microbiota of pRD patients and *Rag1*$^{w/w}$ mice is characterized by a severe restriction of microbial diversity with specific microbial signatures. (A)** Alpha diversity in human fecal microbiota from healthy donors (HD, *n* = 23) and patients with pRD (*n* = 15). Significance was determined by a Kruskal–Wallis chi-squared test. **(B–D)** Relative abundance of oral bacteria (B), *Ruminococcaceae* (C), and Butyricicoccus and Coprococcus (D) in human fecal microbiota from HD (*n* = 23) and patients with pRD (*n* = 15). Significance was determined by a Kruskal–Wallis chi-squared test. **(E)** Principal Coordinates Analysis (PCoA) using the Euclidean distance of the IgA scores of human fecal microbiota from HD, patients with pRD, and patients with pRD and IBD. **(F)** IgA

scores of *Coprococcus*, *Butyricicoccus*, and *Faecalibacterium* from human fecal microbiota of HD and pRD patients. Significance was determined by a Kruskal–Wallis chi-squared test. **(G)** Alpha diversity of fecal microbiota from littermate wild-type (+/+, *n* = 4) or *Rag1*$^{w/w}$ (W/W, *n* = 11) mice kept in co-housing conditions and profiled at 12 wk of age by 16S rRNA gene sequencing. Significance was determined by a Kruskal–Wallis chi-squared test. **(H)** Time course analysis of Shannon index alpha diversity of fecal microbiota from littermate +/+ or W/W mice collected from isolated mice at 3, 5, 10, and 14 wk of age (*n* = 5/group). **(I)** Relative abundance of *Ruminococcaceae* in the fecal microbiota of +/+ or W/W mice collected from isolated mice at 3, 5, 10, and 14 wk of age (*n* =5/group). Significance in H and I was determined by the linear mixed-effects model Shannon ~Genotype + AgeInWeeks + (1|SubjectID) with the lmerTest R package. **(J)** PCoA using the Euclidean distance of the IgA scores of murine fecal microbiota from +/+ (*n* = 8) and W/W mice (*n* = 7). **(K)** IgA scores of Ruminococcaceae from fecal microbiota from +/+ (*n* = 8) and W/W (*n* = 7) mice. Significance was determined by a Kruskal–Wallis chi-squared test. **(L)** Median relative abundance of taxa contributing to PICRUSt-inferred pathways whose abundance is significantly (FDR < 0.05) different between W/W and +/+ mice fecal microbiota (*n* = 5/group). **(M)** Parallel univariate analysis comparing the fecal metabolome of W/W mice to +/+ mice (*n* = 5/group) with notable metabolite families highlighted by color. FDR levels as calculated via a Benjamini–Hochberg correction are indicated. Data are from at least two independent experiments. *P < 0.05, **P < 0.01, ****P < 0.0001. HD, healthy donors.

levels in patients with SCID and OS but residual functional activity in pRD patients (Bosticardo et al., 2025). By applying a multiomics approach to a large group of *RAG*-mutated patients, we have recently shown that pRD is associated with a type 1 immune profile both in blood and in tissues (Bosticardo et al., 2025). Taking advantage of our *Rag1*$^{w/w}$ mouse model, which recapitulates the immunological phenotype seen in pRD patients (Ott de Bruin et al., 2018), we were able to dissect the gut immunopathological signatures, and demonstrated an LP CD4$^+$ T cell infiltrate with an immunological phenotype and transcriptional profile consistent with Th1/Th17 inflammatory signatures, T cell activation, and oligoclonal T cell expansions with molecular signatures of self-reactivity. Of note, IFN-γ– and IL-17–mediated inflammation has been extensively described in IBD pathogenesis, with synergistic action of Th1 and pathogenic Th17 cells in promoting disease development and facilitating aggravation of the mucosal inflammation (Cao et al., 2023). A similar systemic inflammatory signature has been previously demonstrated in patients with OS (a condition characterized by the oligoclonal expansion of activated T cells) (Rigoni et al., 2020) and in the GI tract of a mouse model of this disease (Rigoni et al., 2016). Our study extends this phenotype to pRD and suggests a role for dysregulated T cells in driving organ-specific inflammation. Interestingly, although systemic and tissue-specific inflammatory signatures are already present early in life in *Rag1*$^{w/w}$ mice, their colonic inflammation manifests histologically only after weaning. It has been demonstrated that at weaning, the gut microbiota induces a vigorous immune response, the so-called "weaning reaction," that is fundamental for the physiological immune maturation (Al Nabhani et al., 2019). In particular, this weaning reaction is associated with induction of pTregs and development of peripheral tolerance, and its perturbation has been linked to increased susceptibility to immune-mediated diseases later in life (Al Nabhani et al., 2019). We hypothesize that the genetically determined restriction of TCR repertoire in mice and humans with hypomorphic *RAG* variants may cause an aberrant weaning reaction, ultimately leading to altered composition of gut microbiota. Indeed, *Rag1*$^{w/w}$ mice showed a significantly reduced alpha diversity of gut microbiota composition even when co-housed with wild-type and heterozygous littermates, thus overriding the partial normalization of gut microbiota composition and diversity that is typically observed in co-housing (Robertson et al., 2019). Analysis of the fecal microbiota of pRD patients revealed a relative increase in oral pathogenic bacteria that can drive Th1 induction and severe gut inflammation in the context of a genetically susceptible host (Atarashi et al., 2017). The reduction of SCFA-producing bacteria with concomitant lower levels of SCFA in stool specimens represents the major link between the microbial and immunopathological signatures (Mann et al., 2024). In particular, butyrate, propionate, and acetate, three fermentation by-products of fiber digestion, signal through G protein–coupled receptors (GPCRs); activation of GPR43 by SCFAs promotes pTreg generation and suppressive function (Smith et al., 2013). Furthermore, butyrate-mediated activation of the GPCR GPR109A expressed by CD103$^+$ dendritic cells induces the development of GI tract *Rorc*$^+$ Treg cells, promoting oral tolerance and protecting from food allergy (Tan et al., 2016). Finally, butyrate and propionate inhibit histone deacetylase and at low concentration can enhance histone acetylation (Lund et al., 2022), thereby inducing epigenetic changes at the *Foxp3* locus that facilitate intestinal Treg cell differentiation (Arpaia et al., 2013; Furusawa et al., 2013). It has been recently demonstrated that the GI LP is the key microniche that supports generation and function of *Il10*$^+$ *Rorc*$^+$ effector Treg cells (Gu et al., 2024). In particular, commensal antigens induce the generation of colonic *Rorc*$^+$ Tregs, which have been shown to dampen IFN-γ– and IL-17–mediated pro-inflammatory responses of Teff cells (Sefik et al., 2015; Xu et al., 2018) and to suppress Th2-mediated responses to dietary antigens (Abdel-Gadir et al., 2019) and parasites (Ohnmacht et al., 2015). Accordingly, the loss of *Rorc*$^+$/*Maf*$^+$ Tregs in mice is associated with dysbiosis, lethal oxazolone-induced colitis, increased levels of IgE, and severe allergy (Abdel-Gadir et al., 2019; Ohnmacht et al., 2015). IL-10 has a fundamental role as tolerogenic cytokine, and its depletion has been associated with colitis development (Murai et al., 2009). It has been recently shown that a subpopulation of effector Tregs stably expressing IL-10 is indispensable to maintain colonic health (Dikiy et al., 2025). Our data show that the decrease in SCFA-producing microbial species that becomes manifest after weaning in *Rag1*$^{w/w}$ mice is associated with a reduction in SCFA-dependent *Rorc*$^+$/*Maf*$^+$ *Il10*$^+$ peripheral effector Treg cells, thereby altering mechanisms of immune homeostasis and promoting colonic inflammation. In this pro-inflammatory environment, the exposure to colonic microbes may favor the development of inflammation with an increased number of Th1/Th17 cells infiltrating the LP, as observed in *Rag1*$^{w/w}$ mice. Additionally, analysis of the TCR repertoire has shown that LP CD4$^+$ T cells from

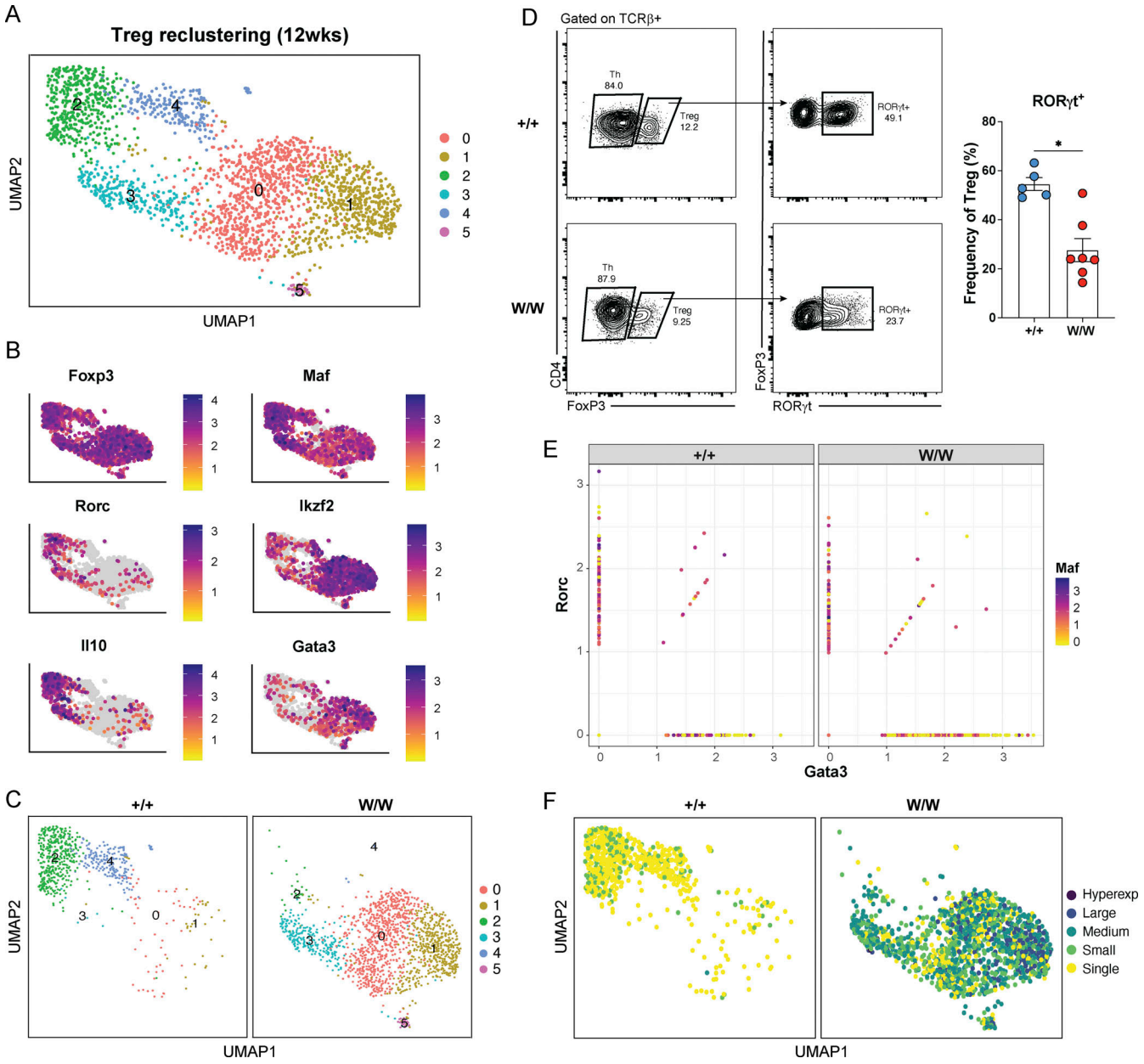

Figure 5. **Decrease in butyrate-producing bacteria and alterations in metabolome correlate with skewed Tregs in partial Rag1 deficiency. (A)** UMAP plot of subclustered Tregs from wild-type (+/+) and *Rag1*$^{w/w}$ (W/W) mice at 12 wk of age. Colors represent cells clustered together on the basis of similarity of global gene expression. **(B)** Feature plots show single-cell gene expression levels of selected genes projected on the UMAP. **(C)** Treg UMAP split by genotype contribution. **(D)** Representative plots and quantification of RORγt$^+$ Tregs in littermate +/+ (n = 5) and W/W mice (n = 7) at 12 wk of age. All flow plots were gated on live CD45$^+$CD90.2$^+$TCRβ$^+$. **(E)** Scatter plot shows co-expression analysis of *Rorc*, *Gata3*, and *Maf* on single cells derived from the subclustered Tregs from +/+ and W/W mice at 12 wk of age. **(F)** TCR clonotype analysis projected on UMAP shows the distribution of different clonotype abundance ranges (single: 1 cell; small: 2–5 cells; medium: 6–20 cells; large: 21–100 cells; and hyperexpanded: 101–500 cells) of reclustered Tregs from the colonic LP of +/+ or W/W at 12 wk of age and analyzed by scRNA-seq. Single-cell samples were obtained from four to five pooled mice/group. Data are from at least two independent experiments. *P < 0.05.

Rag1$^{w/w}$ mice are enriched in clonotypes containing hydrophobic amino acids at the center of the TRB CDR3 region, a biomarker of self-reactive T cells. Purging of T cells expressing TCR chains with increased frequency of hydrophobic amino acids in their CDR3 occurs in the thymus as a result of high-strength interaction between the TCR and self-peptide/MHC (Stadinski et al., 2016). We have previously shown that peripheral blood conventional CD4$^+$ T cells from RAG-mutated patients and *Rag1*$^{w/w}$ mice contain a high frequency of clonotypes with hydrophobic amino acids in the TRB CDR3 (Daley et al., 2019; Rowe et al., 2017). These data suggest that pRD is characterized by failure of negative selection and increased thymic output of oligoclonal and self-reactive T cells, which may trigger peripheral tissue damage. The demonstration that oligoclonal expansions of Th1/Th17 cells can be detected in the LP of *Rag1*$^{w/w}$ mice already at weaning strongly indicates that

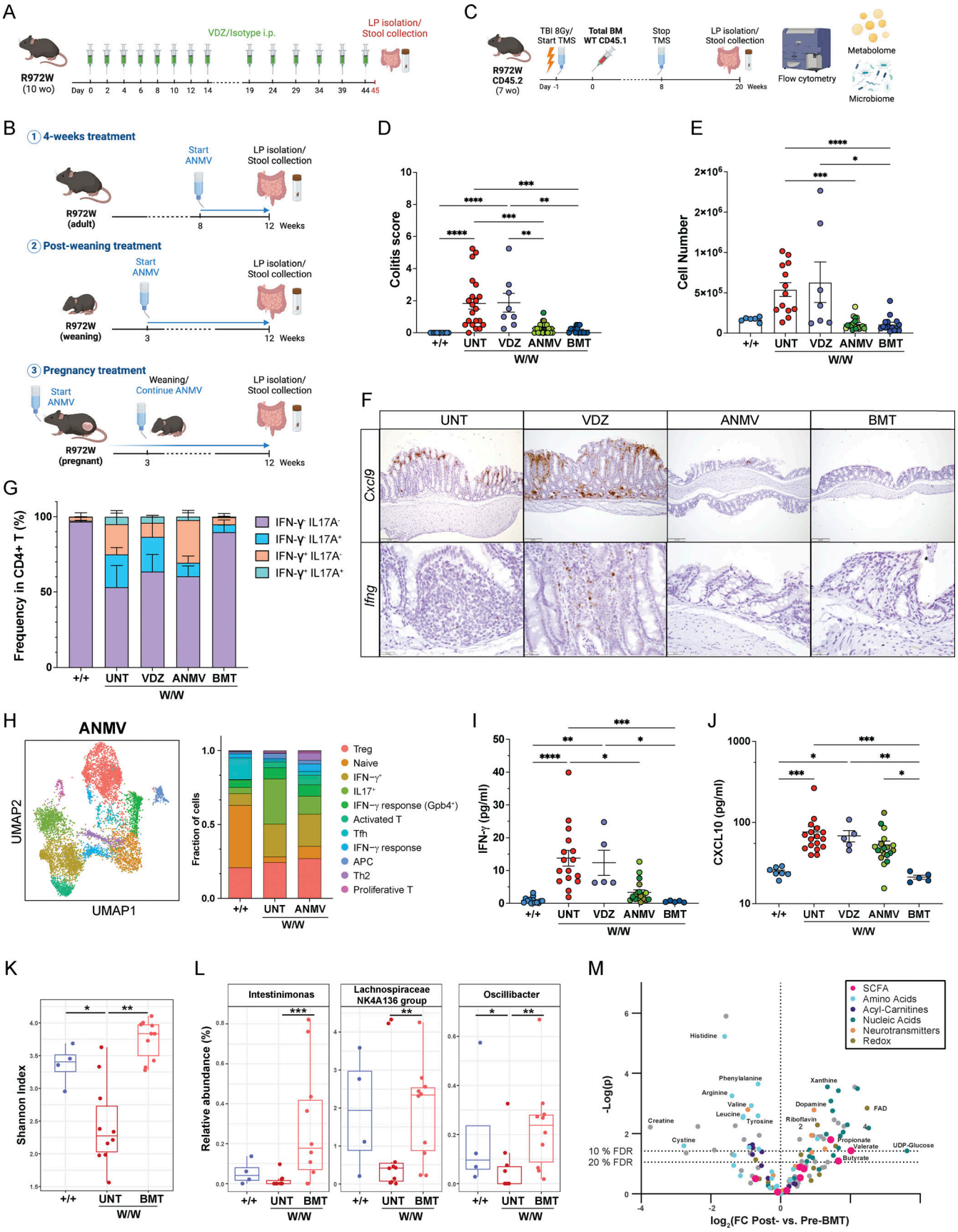

Figure 6. **Different treatments have distinct effects on microbiota and immune cells. (A–C)** Experimental plan of vedolizumab treatment (A), antibiotic regimen (B), and BMT (C) in *Rag1*$^{w/w}$ (W/W) mice. **(D)** Colitis score based on immunohistochemical analysis of 12-wk-old wild-type (+/+, *n* = 15), and W/W mice

untreated (UNT, *n* = 20), or treated with VDZ (*n* = 8), antibiotics (ANMV, *n* = 15), or BMT (*n* = 15). Bars show the mean with SEM. **(E)** Bar plots showing absolute counts of total TCRβ$^+$ T cells isolated from the LP of 12-wk-old +/+ mice (*n* = 15), and W/W mice left untreated (UNT, *n* = 20), or treated with VDZ (*n* = 8), antibiotics (ANMV, *n* = 15), or BMT (*n* = 15). Bars show the mean with SEM. **(F)** RNAscope analysis of colon biopsy isolated from untreated W/W mice, or mice treated with VDZ, ANMV, or BMT showing *Ifng* (40×, scale bar: 20 µm) and *Cxcl9* transcript expression (10×, scale bar: 100 µm). **(G)** Subset distribution of cytokine production by Th cells after restimulation isolated from the LP of 12-wk-old +/+ mice (*n*= 15), and W/W mice left untreated (UNT, *n* = 20), or treated with VDZ (*n* = 8), antibiotics (ANMV, *n* = 15), or BMT (*n* = 15). **(H)** UMAP plot (left panel) showing the expression profiles of CD4$^+$ T cells isolated from ANMV-treated W/W mice. Colors represent cells clustered together on the basis of similarity of global gene expression. The stacked bar plot (right panel) shows cluster distribution in each condition. Single-cell samples were obtained from four to five pooled mice/group. **(I and J)** Serum levels of IFN-γ (I) and CXCL10 (J) of 12-wk-old +/+ mice (*n*= 7), and W/W mice left untreated (UNT, *n* = 17), or treated with VDZ (*n* = 5), antibiotics (ANMV, *n* = 19), or BMT (*n* = 5). Error bars show the mean with SEM. **(K)** Alpha diversity of fecal microbiota collected from +/+ (*n* = 4) or W/W mice before (UNT, *n* = 10) and after BMT (*n* = 10). Significance was determined by a Wilcoxon rank test. **(L)** Relative abundance of Firmicutes in the fecal microbiota from +/+ (*n* = 4) or W/W mice before (UNT, *n* = 10) and after BMT (*n* = 10). Significance was computed from the linear mixed-effects model ~Group + (1|SubjectID) using the MaASLin2 R package. **(M)** Parallel univariate analysis comparing the fecal metabolomes of W/W mice after BMT to before BMT (*n* = 10/group) with notable metabolite families highlighted by color. FDR levels as calculated via a Benjamini–Hochberg correction are indicated. +/+ mice were internally bred (C57BL/6J [CD45.2] or B6.SJL-Ptprca Pepcb/BoyJ [CD45.1]). Data are from more than three independent experiments. Groups were compared using a Kruskal–Wallis test with Dunn's multiple comparisons correction (B, E, and G). *P < 0.05, **P < 0.01, ***P < 0.001, ****P < 0.0001. VDZ, vedolizumab.

this pro-inflammatory signature is microbiota-independent and rather genetically driven.

Several lines of evidence indicate that alterations of TCR repertoire (with restricted diversity and oligoclonal expansion of inflammatory and dysreactive clonotypes) play a critical role in the development of IBD. First, contrary to what observed in *Rag1*$^{w/w}$ mice, no spontaneous development of inflammatory gut disease is observed in *Rag*$^{-/-}$ mice (Aranda et al., 1997), which can be induced upon transfer of naïve CD4$^+$CD45RB^{high} T cells from wild-type mice into *Rag1*$^{-/-}$ or *Rag2*$^{-/-}$ mice (Reinoso Webb et al., 2018). Moreover, adoptive transfer of total CD4$^+$ cells from MLN of *Rag2*$^{R229Q/R229Q}$ mice (mimicking OS) into *Rag1*$^{-/-}$ recipients reproduced the IBD observed in *Rag2*$^{R229Q/R229Q}$ mice, whereas adoptive transfer of wild-type Treg cells into *Rag2*$^{R229Q/R229Q}$ mice improved bowel inflammation (Rigoni et al., 2016). To further confirm the importance of T cells in maintaining homeostatic interactions with the microbiota, intestinal inflammation was a prominent feature of a mouse model of partial Lck deficiency affecting T, but not B, cell development and function (Lui et al., 2024). Of note, consistent with our findings, Lui et al. demonstrated that complete versus partial loss-of-function LCK in mouse models causes disease with differing phenotypes. While both mouse models showed an arrest in thymic T cell development and profound T cell lymphopenia, only mice with partial loss of function exhibited residual T cell proliferation and intestinal inflammation. Furthermore, the intestinal disease in mice with partial loss of function was prevented by CD4$^+$ T cell depletion or by transfer of regulatory T cells. These findings suggest that partial loss-of-function LCK spares sufficient T cell function to allow the maturation of some conventional T cells but not regulatory T cells—leading to intestinal inflammation. Finally, in humans, IBD is not observed in patients with RAG-deficient SCID, but is frequently detected in patients with OS due to oligoclonal expansion of activated autologous T cells (Rigoni et al., 2020).

Defects of humoral immunity may also contribute to the immune dysregulation of pRD. We have confirmed that patients with pRD manifest B cell lymphopenia. While several of them had normal or low-normal IgM and IgA levels, previous studies from our group and others have shown that restriction of the BCR repertoire is another cardinal feature of pRD (Csomos et al., 2022; Lee et al., 2016). Similar features have been observed in *Rag1*$^{w/w}$ mice (Ott de Bruin et al., 2018). Furthermore, the B cell compartment of both pRD patients and *Rag1*$^{w/w}$ mice is enriched in dysreactive B cells (Bosticardo et al., 2025; Csomos et al., 2022; Ott de Bruin et al., 2018), which may further contribute to autoimmune manifestations. To investigate the possible contribution of impaired humoral immune responses to intestinal inflammation, we have performed IgA-seq profiling of fecal microbiota in pRD patient and *Rag1*$^{w/w}$ mice. Production of IgA against small intestine–resident bacteria has been shown to promote colonization with bacteria promoting homeostasis and eubiosis. IgA-seq profiling demonstrated the reduced presence of IgA-coated *Ruminococcaceae* both in pRD patients and in *Rag1*$^{w/w}$ mice compared with controls. This may affect the capacity of *Ruminococcaceae* to tether to the mucus and hence to colonize the gut, accounting for the reduced relative abundance of this family in the fecal microbiome.

In this study, we explored multiple approaches to prevent or treat IBD associated with pRD. Despite the efficacy of vedolizumab in treating ulcerative colitis and Crohn's disease (Wyant et al., 2016), the use of this drug was ineffective in *Rag1*$^{w/w}$ mice. It has been previously shown that vedolizumab may be beneficial to prevent IBD in a SCID T cell transfer model of colitis if administered starting at the same day of T cell transfer, but did not improve intestinal inflammation if administered 3 wk after T cell transfer (Lindebo Holm et al., 2012). Negative results were also observed upon administration of ustekinumab, targeting both IFN-γ and IL-17 production, in one patient with pRD. In this case, despite an increase in the frequency of administration of the drug, worsening of intestinal inflammation was observed. Although limited to a single case, this observation suggests that targeting of IFN-γ and IL-17 production is insufficient to control inflammation. We speculate that interfering with cytokine production or with T cell trafficking without correcting T cell function and diversity of the TCR repertoire may be detrimental, and may in fact aggravate the inability to adequately control the microbial burden.

Interestingly, the use of antibiotics was associated with improvement of inflammatory signatures in the GI tract of *Rag1*$^{w/w}$ mice. We speculate that by depleting pathogenic bacteria, the use of antibiotics may have beneficial effects on dysbiosis, and

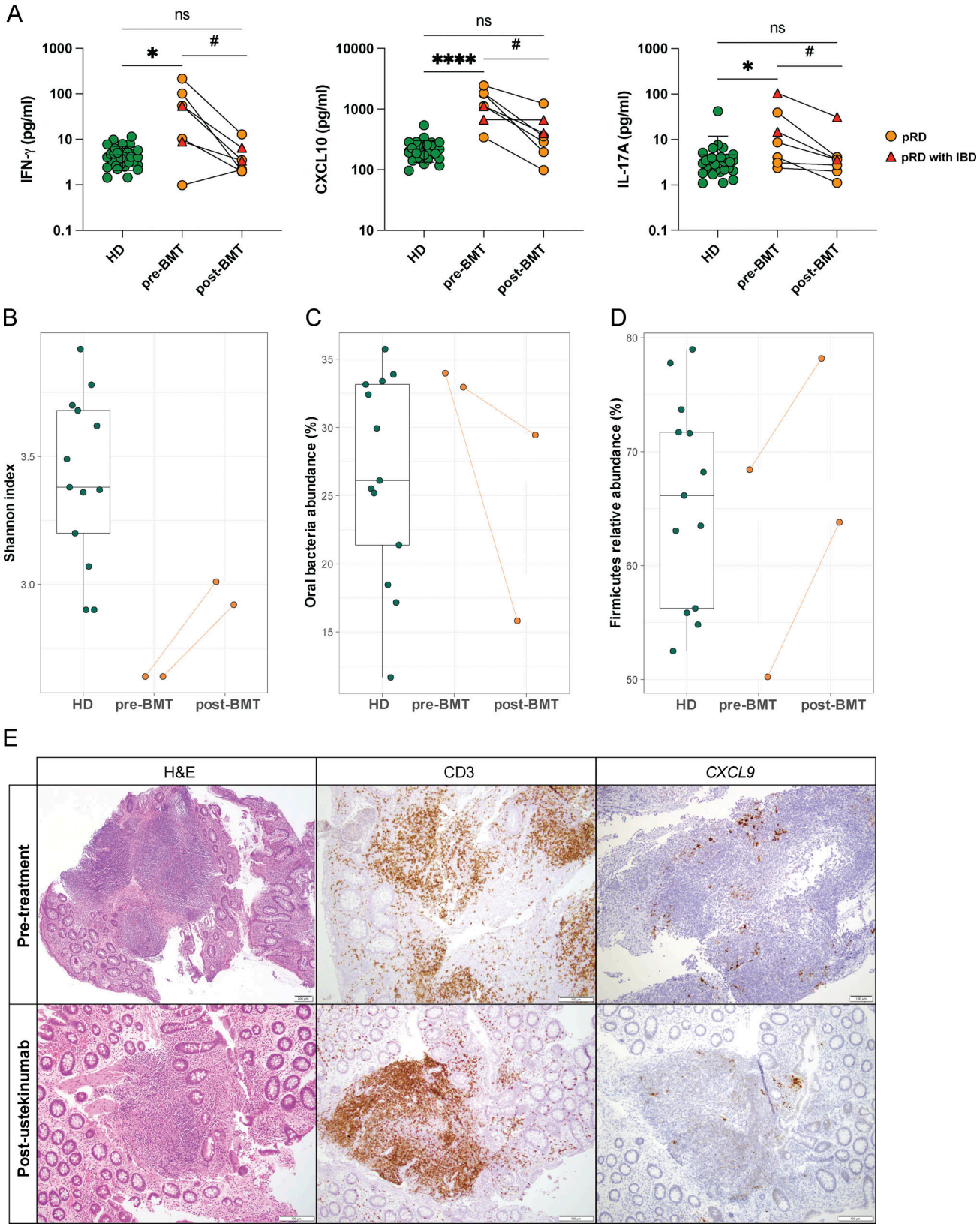

Figure 7. **Resolution of systemic inflammatory signatures and improvement of fecal microbiota composition after BMT, and persistence of colonic inflammation after ustekinumab in pRD patients. (A)** Scatter plots (mean with SD) showing serum cytokine levels in HD (n = 29) and patients with pRD (n = 7) before and after BMT. Red triangles indicate pRD subjects with IBD. Statistical analysis was performed using a Kruskal–Wallis test to compare HD with pRD before and after BMT (*P < 0.05, ****P < 0.0001), while a paired Wilcoxon test was used to compare pRD before and after BMT (#P < 0.05). **(B)** Alpha diversity in human fecal microbiota from HD (n = 23) and patients with pRD before and after BMT (n = 2). **(C and D)** Relative abundance of oral bacteria (C) and of

Ruminococcaceae (D) in human fecal microbiota from HD (n = 23) and patients with pRD before and after BMT (n = 2). **(E)** Immunohistochemical analysis of colon biopsy isolated from one pRD patient (P3) before and after treatment with ustekinumab, showing H&E and CD3 staining, as well as RNAscope analysis for the expression of *CXCL9* transcript. All images are 10× magnification (scale bar for H&E pretreatments is 200 µm; other scale bars are 100 µm). HD, healthy donors.

hence also on the induction of pathogenic T cell responses. However, antibiotics do not correct the genetically determined skewing of Th profile nor the restriction of TCR repertoire. While they may help dampen inflammation in patients with pRD, they are insufficient to correct the disease.

BMT is the treatment of choice to normalize adaptive immune responses in pRD (Schuetz et al., 2023). Our study demonstrates that it is also successful in correcting the genetically determined immune dysregulation in the GI tract and dysbiosis associated with hypomorphic forms of the disease. The use of BMT in *Rag1*$^{w/w}$ mice led to resolution of T cell infiltrate in the colon, normalization of the microbiome composition, and restoration of SCFA levels. Our preliminary results confirm the beneficial effects of BMT also in pRD patients, allowing complete resolution of clinical and laboratory features of IBD. The outcome of BMT in pRD is superior when performed early in the course of the disease, and especially in patients with positive newborn screening, whereas organ damage is predictive of worse outcome when transplantation is performed in adulthood (Schuetz et al., 2023).

Despite the caveats that should be acknowledged when comparing human and murine gut microbiota (Nguyen et al., 2015), our data demonstrate that pRD patients and *Rag1*$^{w/w}$ mice share common microbial signatures, indicating that *Rag1*$^{w/w}$ mice may represent a valuable model to study the pathophysiology of the chronic colitis identified in pRD patients.

Overall, by applying and integrating an array of multiple approaches to a cohort of pRD patients and a corresponding mouse model, we dissected the immunopathological, microbial, and metabolomic signatures associated with IBD in pRD. Our findings shed new light in the pathophysiology of intestinal disorders in patients with hypomorphic *RAG* mutations and establish a curative role for BMT in fully resolving the disease phenotype, which could possibly extend to other genetically determined immune dysregulation disorders characterized by a restricted TCR repertoire.

Materials and methods

Patients

The study included 16 patients with biallelic *RAG* variants causing pRD, manifesting as combined immune deficiency (13/16, 80%) or leaky SCID (3/16, 20%). Characteristics of the patients' clinical and immunological phenotype are reported in Table 1. Moreover, serum from 32 HC (17 adult and 15 pediatric HC) was analyzed for the measurement of soluble biomarkers and stool specimens from 23 HC (age-matched and corrected for the specific household) were studied for the fecal microbiota characterization. Blood and stool specimens from patients and controls and colonic tissue samples from patients were obtained upon informed consent, according to protocols 18-I-0041 (NCT03394053 in https://clinicaltrials.gov) and 18-I-0128 (NCT03610802), approved by the National Institutes of Health Institutional Review Board, and to protocol 00035468, approved by the University of South Florida Institutional Review Board.

Mice

Rag1$^{w/w}$ mice were generated by gene editing as previously described (Ott de Bruin et al., 2016). Animal work was conducted in accordance with the U.S. Public Health Service Policy on Humane Care and Use of Laboratory Animals, with protocols approved by the National Institute of Allergy and Infectious Diseases Animal Care and Use Committee (protocol LCIM 6E). Mice were group-housed (four to five mice of the same sex per cage) in a controlled environment with unrestricted access to water and a standard chow diet. Moreover, for specific sets of experiments (as detailed in the specific figure legends), we isolated *Rag1*$^{w/w}$ mice from wild-type mice immediately after weaning, avoiding possible microbial contamination among the two groups due to cage-sharing and murine coprophagy.

Regarding the treatment strategies, ANMV antibiotic cocktail, vedolizumab, and BMT were tested. Mice received the ANMV antibiotic cocktail consisting of ampicillin 1 g/liter, neomycin 1 g/liter, metronidazole 1 g/liter, and vancomycin 0.5 g/liter in drinking water ad libitum. The antibiotic solution was changed three times a week. ANMV was given with three different approaches: (1) for 4 wk (8–12 wk of age), (2) starting at 3 wk of age until sacrifice at 12 wk of age, or (3) at pregnant mothers, to expose the mice to antibiotics from fetal life to sacrifice at 12 wk of age. Water intake was monitored throughout the antibiotic administration. For the mice receiving ANMV for 4 wk, following completion of the antibiotic administration phase, regular drinking water was provided ad libitum for the remainder of the experiment.

10-wk-old *Rag1*$^{w/w}$ mice received 200 µg of vedolizumab (InVivoMAb anti-mouse LPAM-1) or of isotype control (InVivoMAb rat IgG2a isotype control) every 2 days for 2 wk and then every 5 days until sacrifice after 45 days from treatment initiation (Lindebo Holm et al., 2012; Rosser et al., 2014; Sheridan et al., 2014).

For BMT experiments, 7-wk-old *Rag1*$^{w/w}$ mice received TBI (8 Gy) 1 day before transplantation. On the day of transplantation, total BM cells were obtained from 6- to 10-wk-old donor CD45.1 C57BL/6 wild-type mice and administered intravenously to *Rag1*$^{w/w}$ mice at a dose of 2 × 10^7 cells. Of note, antibiotic TMS water was initiated after TBI and interrupted after 8 wk. BMT-transplanted mice were sacrificed after 20 wk from BMT (27 wk of age).

Mouse histology

Mouse colonic tissue samples were formalin-fixed and paraffin-embedded. Sections (1.5 µm) were used for routine H&E staining

to check for basic histopathological changes. Sections were dewaxed and rehydrated, endogenous peroxidase activity was blocked by 0.1% H_2O_2 for 15 min, and nonspecific background was reduced with Rodent Block (Biocare Medical) for 30 min before microwave antigen-retrieval treatment (EDTA buffer, pH 8.0). Moreover, sections were incubated for 1 h at room temperature with the primary rabbit polyclonal antibody anti-CD3 (1:100; Thermo Fisher Scientific) and then incubated for 30 min with MACH 1 Universal HRP Polymer Kit (Biocare Medical). In the end, reactions were developed in Biocare's Betazoid DAB and nuclei counterstained with hematoxylin.

Digital images were acquired by an Olympus XC50 camera mounted on a BX51 microscope (Olympus), with CellF Imaging software (Soft Imaging System GmbH). A previously reported gut histologic score (colitis score) (Rigoni et al., 2016) was adopted by a pathologist (E. Fontana) for evaluating blindly different severity degrees of inflammation: grade of inflammation (scoring from 0 to 4, where 0 is normal condition and 4 is a severe grade of inflammation), the structural changes of the glands (scoring from 0 to 3, where 0 is normal condition and 3 is severe structural changes), and the goblet cell alterations (scoring from 0 to 3, where 0 is normal condition and 3 is severe alterations).

Human histology and in situ hybridization–based detection of human and mouse *CXCL9* and *IFNG*

All slides were baked for 60 min prior to staining. The manual RNAscope 2.5 High Definition—BROWN assay kit (Cat No. 322300; Advanced Cell Diagnostics, Inc. [ACD]) was used according to the manufacturer's instructions to perform in situ hybridization for Hs-*CXCL9* Probe (Cat No. 440161), Hs-*IFNG* Probe (Cat No. 310501), Mm-*Cxcl9* Probe (Cat No. 489341), and Mm-*Ifng* Probe (Cat No. 311391) on formalin-fixed paraffin-embedded (FFPE) tissue sections (Wang et al., 2012).

Slides were deparaffinized in xylene (2 × 5 min), dehydrated in 100% EtOH (2 × 1 min), air-dried at room temperature (RT), and incubated in RNAscope Hydrogen Peroxide (Cat No. 322330; ACD) at RT for 10 min to quench endogenous peroxidases. Slides were washed in deionized (DI) water twice before being submerged in 700 ml of fresh boiling RNAscope 1X Target Retrieval Reagents solution (Cat No. 322000; ACD) for 15 min, and then washed twice in DI water, once in 100% EtOH, and air-dried at RT. A hydrophobic barrier was drawn around the tissue, and RNAscope Protease Plus (Cat No. 322330; ACD) was applied for 20 min in a HybEZ Oven at 40°C (ACD). Slides were then washed twice in DI water and incubated with the appropriate probe for 2 h in the HybEZ Oven. RNAscope signal amplification reagents (Cat No. 322310; ACD) AMP 1 (30 min), AMP 2 (15 min), AMP 3 (30 min), AMP 4 (15 min), AMP 5 (75 min), and AMP 6 (15 min) were applied and incubated in HybEZ Oven. Before adding each AMP reagent, the slides were washed twice with RNAscope 1X Wash Buffer (Cat No. 310091; ACD). After removing AMP 6, slides were washed twice in wash buffer and RNAscope DAB detection reagents (Cat No. 322310; ACD) were applied and incubated for 10 min in HybEZ Oven. Sections were washed in tap water, counterstained with Harris–Mayer's hematoxylin, washed again in tap water, placed in 0.02% ammonia water for 10 s, and washed a final time with tap water. Sections were then dehydrated in graded alcohols, treated with xylene (2 × 5 min), and coverslipped.

Immunohistochemical evaluation of FFPE for CD3

All slides were baked prior to staining. CD3 immunohistochemical staining was performed on an automated immunostainer BenchMark Ultra (Roche). After baking, Ultra CC1 (Cat No. 950-224; Roche) was applied to the slide for a 64-min antigen retrieval. Predilute CD3 (Clone 2GV6, Cat No. 790-4341; Ventana) was incubated for 32 min and detected with ultraView Universal DAB Detection Kit (Cat No. 760-500; Roche). Hematoxylin was used to counterstain. The slides were dehydrated in graded alcohols, treated with xylene (2 × 5 min), and coverslipped. Images were taken with an Olympus Bx41 microscope, objective UPLanFI 10×/0.30, 20×/0.50 ∞/0.17, 40×/0.75∞/0.17, and 100×/1.30 oil with an adaptor U-TV0.5xC using an Olympus DP27 camera with an Olympus U-VTO.63xC adaptor, using CellSens, XV Image Processing, imported into Adobe Photoshop CC 2024.

Measurement of soluble biomarkers in mouse samples

Cytokine and chemokine biomarker analysis was performed on sera obtained from wild-type and *Rag1*$^{w/w}$ mice. Aliquots were stored in a −85°C freezer prior to analysis. Cytokines (IFN-γ, IL-1β, IL-2, IL-4, IL-5, IL-6, IL-9, IL-10, IL-12p70, IL-15, IL-17A/F, IL-27p28/IL-30, IL-33, IP-10, KC/GRO, MCP-1, MIP-1α, MIP-2, TNF-α) were measured using V-PLEX Mouse Cytokine 19-Plex Kit (Meso Scale Discovery) and analyzed on a MESO QuickPlex SQ 120 reader (Meso Scale Discovery) according to the manufacturer's specifications. Standard curves were analyzed using nonlinear curve fitting, and unknowns were calculated based on the derived equation. Duplicate determinations yielded coefficients of variation that were normally <10%. Defined low, medium, and high control samples were run on each plate to validate the responses and to assess the interplate variation. Cytokine values from the control samples had <5% plate-to-plate variation and averaged 100.7% (range 83.1–147.4) of their expected values.

Measurement of soluble biomarkers in human samples

Analysis of soluble biomarker plasma levels was performed in RAG patients and in healthy donors using V-PLEX Human Cytokine 30-Plex Kit (Meso Scale Discovery) and a MESO QuickPlex SQ 120 reader (Meso Scale Discovery) or using a customized, magnetic bead-based, multiplex assay (R&D Systems), depending on the nature of the analyte, as previously described (Sacco et al., 2022).

Determination of CXCL9 concentrations in mouse and human sera

The mouse and human CXCL9 DuoSet ELISA kits (R&D) were used to determine the concentration of CXCL9 in sera from healthy donors and RAG patients and wild-type and *Rag1*$^{w/w}$ mice according to the manufacturer's instructions.

LP mononuclear cell isolation

Mice were euthanized with CO_2, and the colon was collected and placed into cold complete medium (RPMI 1640 supplemented

with 2 mM L-glutamine, 1 mM sodium pyruvate, 1 mM nonessential amino acids, 20 mM HEPES, 50 mM β-mercaptoethanol, 100 U/ml penicillin, and 100 mg/ml streptomycin). For colonic LP preparation, the mesenteric adipose tissue was removed. Tissues were opened, washed in cold PBS to remove feces, cut into 1- to 2-cm segments, and treated with complete medium containing 5 mM EDTA and 0.145 mg/ml dithiothreitol for 20 min at 37°C with constant stirring. Tissues were shaken vigorously for 1 min and further digested with 10 ml of medium containing 500 mg/ml DNase I (Sigma-Aldrich) and 100 mg/ml Liberase TL (Roche) with continuous stirring at 37°C. Digested tissues were passed through 70-µm cell strainers. Leukocytes were enriched by resuspension in 4 ml of 37.5% Percoll and centrifuged at 400 g for 5 min. Cells were then washed with PBS before downstream analysis.

In vitro restimulation

To assess cytokine production potential, single-cell suspensions were restimulated in complete medium containing 10% fetal bovine serum, 50 ng/ml phorbol myristate acetate (Sigma-Aldrich), 5 mg/ml ionomycin (Sigma-Aldrich), and a 1:1,000 dilution of GolgiPlug (BD Biosciences) for 2.5 h at 37°C.

Flow cytometry analysis

The following fluorochrome-labeled antibodies were used for flow cytometry studies: PE-CF594 anti-B220, BUV737 anti-CD11b, PE-CF594 anti-NK1.1, BV421 anti-SiglecF, PE-CF594 anti-TCRβ, BUV737 anti-TCRβ, PE-CF594 anti-TCRγδ (all from BD Horizon); PerCP-Cy5.5 anti-CD103, PerCP-Cy5.5 anti-CD11c, APC-eF780 anti-CD45, PE-Cy7 anti-CD45, FITC anti-FoxP3, eF660 anti-GATA3, AF700 anti-MHC-II, PE anti-RORγT, PerCP-Cy5.5 anti-TNF-α (all from Invitrogen); BV510 anti-CD4, Pacific Blue anti-CD4, BV510 anti-CD45, APC-Cy7 anti-CD45.1, BV510 anti-CD45.2, APC anti-CD45.2, PE anti-CD62L, APC anti-CD64, PerCP-Cy5.5 anti-CD8α, AF700 anti-CD90.2, PerCP-Cy5.5 anti-GATA3, BV605 anti-IFN-γ, PE-Cy7 anti-IL-17A, APC anti-LPAM-1, BV605 anti-Ly6C, BV421 anti-T-BET (all from BioLegend); AF700 anti-CD3ε, APC-Cy7 anti-CD44, PE-Cy7 anti-Ly6G (all from BD Pharmingen); FITC anti-CD24 (eBioscience); PE anti-CCR2 (R&D); and BV650 anti-CD8β (BD OptiBuild). For intracellular cytokine and transcription factor staining, after surface staining, cells were fixed and permeabilized using the Foxp3/Transcription Factor Staining Buffer Set (Thermo Fisher Scientific) for at least 1 h at 4°C and stained with fluorophore-conjugated antibodies for at least 1 h at 4°C. All staining was performed in the presence of purified anti-mouse CD16/32 and purified rat gamma globulin.

Colonic tissue qPCR analysis

Total RNA was extracted from 1 cm of colonic tissue. The colonic tissue was homogenized in PureZOL reagent (Bio-Rad Laboratories) using TissueLyser II (Qiagen). RNA was extracted using the RNeasy Lipid Tissue kit (Qiagen), and cDNA was synthesized using the High-Capacity cDNA Reverse Transcription kit (Thermo Fisher Scientific). Quantitative RT-PCR was performed using an RT-PCR system (ViiA 7; Thermo Fisher Scientific) with TaqMan probes. The relative amounts of mRNAs were calculated as $2^{-\Delta CT}$ and expressed as arbitrary units. Each sample was analyzed in duplicate, and the relative level of expression was determined by normalization to β-actin (Actb) ribosomal RNA.

scRNA-seq and TCR repertoire analysis

LP CD4$^+$ T cells (2.5×10^4) were isolated from each sample using a FACSAria II (BD) cell sorter. All samples were labeled with TotalSeqC hashtag antibodies (BioLegend), pooled, and encapsulated into droplets using Chromium Single Cell Controller (10X Genomics), and libraries were prepared using Chromium Single Cell 5′ Reagent Kits v2 (Dual Index) with Mouse TCR Amplification Kit and 5′ Feature Barcode Kit (10X Genomics). The Controller was loaded with 2.5×10^4 cells per lane. mRNA, TCR, and hashtag oligonucleotide (HTO) libraries were prepared following the 10X Genomics user guide. Libraries were sequenced on NextSeq 550, with 10% of the lane occupied by the HTO library, 10% by the TCR library, and 80% by the mRNA library.

Six 10X Chromium mRNA libraries were sequenced in two runs with an average yield of ∼128 million and a total yield of ∼766 million total reads, whereas the average and total number of read pairs sequenced in the six TCR (VDJ) libraries were ∼19 million and ∼113 million, respectively. The overall sequencing quality was high; at least 96% of bases (for both mRNA and VDJ reads) in the barcode regions had Q30 (99.99% inferred base call accuracy) or above, whereas at least 90% of bases in the mRNA and VDJ reads had Q30 or above. Similarly, >95% of the bases in unique molecular identifier (UMI) had Q30 or above for both mRNA and VDJ reads.

Furthermore, the median gene count per cell range was 620–1,978 (17,283–19,595 genes detected per library) along with 53–64% of the reads mapped confidently to the transcriptome, whereas the mean read count per cell was ∼15,000 with an average value of 92% of the reads detected in a total number of 77,422 cells across the six mRNA libraries. The percentage of cells with productive V-J spanning (TRA-TRB) pairs ranged between 65% and 80%, and the mean read pair count per cell was ∼3,600 with an average value of 62.4% of the reads detected in a total number of 37,347 cells in the six VDJ libraries.

The initial processing of the expression data involved generating fastq files and count matrices using Cell Ranger (Zheng et al., 2017) v6.0 (10X Genomics) that was run with the mm10-2020-A transcriptome reference, whereas the TCR data were processed with Cell Ranger v6.0 and the vdj_GRCm38_alts_ensembl-5.0.0 reference. HTO counts were generated using CITE-seq-Count v1.4.3 (https://github.com/Hoohm/CITE-seq-Count) with a mapping rate of 96% to HTO barcodes across the six HTO libraries (∼78 million total reads).

Downstream analysis integrating the mRNA, TCR, and HTO data modalities was carried out using the R packages Seurat v4.1.0 (Hao et al., 2021) (mRNA and HTO) and scRepertoire v1.11.0 (TCR) (Borcherding et al., 2021), respectively. Cells that met all of the following quality control–based criteria were retained for downstream analysis: (1) cells with a minimum gene count of 200 that was set using the min.features parameter of the CreateSeuratObject in Seurat, (2) cells identified as singlets by the R package scDblFinder (v1.8.0 with default settings) that

operates on the RNA assay, (3) cells with a number of median absolute deviations (nmads) < 4 for mitochondrial content and nmads of 3 and 2.5 defining the range of the low and high gene (nFeature_RNA) and UMI (nCount_RNA) counts, respectively, as identified by the isOutlier function of the R package scuttle (v1.4.0), and (4) cells identified as singlets by the HTODemux function (positive.quantile set to "0.95") of Seurat that operates on the HTO assay. The expression data were normalized using the NormalizeData function of Seurat, where the normalization.method parameter was set to "LogNormalize" and "CLR" for RNA and HTO assays, respectively. The integration of the data from individual sequencing libraries was carried out by the FindIntegrationAnchors and IntegrateData (dims parameter set to "1:20" for both) functions of Seurat.

Pairwise differential expression analysis was performed on the log-normalized RNA expression data with the FindMarkers function of Seurat (parameter settings of min.pct: 0.25, test.use: "MAST," min.cells.group:50, and min.diff.pct = 0.2) utilizing Model-based Analysis of Single-cell Transcriptomics (MAST [Finak et al., 2015]), whereas the FindAllMarkers (parameter settings of min.pct = 0.25, test.use = MAST, min.cells.group = 30, min.diff.pct = 0.2) function was used to identify cluster-specific markers that were utilized for cell-type annotation. The FindClusters function of Seurat was used to cluster the cells with the default Louvain clustering setting and a resolution value of 0.3. Enrichment analysis was performed using the R package WebGestaltR (v0.4.5) (Liao et al., 2019).

TCR repertoire sequencing data were analyzed with the scRepertoire package v1.11.0 (Borcherding et al., 2021). Starting with the filtered Cell Ranger contig annotation output, combineTCR and combineExpression functions were used for combining the TCR data from each sequencing library and for integrating the combined TCR data and scRNA-seq datasets, respectively. We utilized scRepertoire along with the amino acid sequence of the paired CDR3 regions of the α and β (TRA-TRB) chains to define each clonotype and to quantify its abundance, whereas pairwise clonotype overlap between different cell populations was based on TRA-only clonotype definitions. Clonotypes were classified into five groups based on their abundance (or size): single (represented by one cell), small (2–5 cells), medium (6–20 cells), large (21–100 cells), and hyperexpanded (101–500 cells). Pairwise clonotype overlap between cell populations was quantified by the Jaccard index, which is the ratio between the number of common (intersection) set of unique clonotype sequences at the amino acid level and the number of combined (union) set of unique clonotype sequences. For hydrophobic index analyses, the conserved TCR Vβ germline-encoded cysteine in CDR3β was defined as position 1 of CDR3β. The hydrophobic index equals the percentage of cells in which positions 6 and 7 (P6-P7) of CDR3β correspond to any of the 175 amino acid doublets identified as promoting self-reactivity when present at P6–P7 of CDR3β (Stadinski et al., 2016). The figures associated with scRNA-seq and TCR analyses were generated using the R packages ggpubr (v0.4.0.999), ggplot2 (v3.4.2), scCustomize (v0.7.0), Seurat (v4.1.0), stringr (v1.5.1), tidyverse (v2.0.0), and clusterProfiler (v4.2.2).

Microbiome analysis

DNA extraction

Murine and human fecal samples were processed separately at each stage of DNA extraction, library preparation, and next-generation sequencing. DNA was extracted from fecal samples in two stages. The first stage consisted of adding 50 mg of fecal sample and MBL lysis buffer (Qiagen PowerMicrobiome DNA/RNA EP Kit) to Lysis Matrix E tubes (MP Biomedicals). Fecal samples were lysed on a Precellys 24 Tissue Homogenizer (Bertin Technologies) and centrifuged, and the resultant supernatant was transferred to a deep 96-well plate. The second stage consisted of DNA isolation from the above supernatant using Qiagen MagAttract PowerMicrobiome DNA/RNA EP Kit on an Eppendorf automated liquid handling system as detailed by the manufacturer.

Library preparation and sequencing

The composition of the bacterial microbiome was assessed using a dual-index amplification and sequencing approach of the V4 region of the 16S ribosomal RNA (16S rRNA) gene on the Illumina MiSeq Platform. This method used the 16S rRNA 515F and 806R primers with individual sample-specific indexes and Illumina sequencing adapters appended as described in Kozich et al., (2013). The V4 was amplified using 5 μM of F/R primers, 1X Phusion High-Fidelity DNA Polymerase (New England Biolabs), and 100 ng of DNA as starting material. PCR conditions for amplification were as follows: initial template denaturation at 98°C for 60 s; 25 cycles of denaturation at 98°C for 10 s, primer annealing 55°C for 30 s, and template extension at 72°C 60 s; and a final template extension at 72°C for 5 min. Final PCR products were isolated using AMPure XP beads (Beckman-Coulter) at a 1:1 ratio.

Final 16S V4 libraries were quantified using KAPA qPCR Library Quantification Kit (Kapa Biosystems) and pooled at an equimolar concentration. Pools were normalized to 8 pM, spiked-in with 15% phiX control library to add sequence diversity to the pool, and sequenced on the Illumina MiSeq instrument utilizing 600-cycle Paired-End (250 × 250) Reagent Plate with the addition of 16S V4-specific sequencing primers as detailed in Kozich et al. (2013).

Raw amplicon sequences were assessed for quality with FastQC (https://www.bioinformatics.babraham.ac.uk/projects/fastqc/) and MultiQC. Additionally, error correction (denoising) and amplicon sequence variant (ASV) calling were done with the DADA2 R package (Callahan et al., 2016) and SILVA taxonomic database v138.1 (Quast et al., 2013). Microbial community analysis was performed in R and additional packages: vegan (diversity) (https://CRAN.R-project.org/package=vegan), MMuPhin v 1.12.1 (batch correction) (https://doi.org/10.18129/B9.bioc.MMUPHin, Ma, 2025), ggplot2 (visualizations) (Wickham, 2016), MaASLin2 (differential abundance) (Mallick et al., 2021), and LmerTest (alpha diversity comparisons) (Kuznetsova et al., 2017). PICRUSt2 v2.4.1 (Douglas et al., 2020) was used for functional inference of the communities based on their taxonomic content in the Nephele application (https://nephele.niaid.nih.gov/pipeline_details/picrust2/).

To identify putative oral taxa in the gut microbiota, taxonomic classification of the ASVs was done with DADA2's rdp function and the Mouse Oral Microbiome Database v5.1 for the mouse samples (Joseph et al., 2021). For the human microbiome samples, SourceTracker2 was used to estimate gut, oral, and skin source fraction of microbial communities between pRD patients and controls. Gut, oral, and skin source communities were downloaded from AGP (https://www.ebi.ac.uk/ena/browser/view/PRJEB11419) with sink rarefication depth set to 1,000. Additionally, the ASVs were classified using the Human Oral Microbiome Database v15.23 (Al-Hebshi et al., 2015).

The raw human microbiome dataset was represented by 1,232 ASVs and 396 species with a sequence depth of samples varying between 9.5K reads and 90.7K reads. ASVs were filtered at relative abundance of 0.01% and prevalence in at least three samples of the dataset. This retained 276 high-quality, well-represented ASVs and 163 species across all samples of the human dataset. The batch effect due to multiple sequencing runs was successfully reduced (from significance of 7%) to a non-significant contribution to community differences (at 5%; MMUPHin).

For the time course study, the raw mouse microbiome dataset was represented by 612 ASVs with a sequence depth ranging between 38,100 and 91,200 reads. After filtering for prevalence of at least 0.1% in five samples, 413 ASVs remained. For the BMT study, there were 426 ASVs, and after filtering, 337 remained.

IgA-seq on mouse and human stool samples

IgA-seq on murine stools was performed as described previously (Vujkovic-Cvijin et al., 2022). Briefly, stool samples were placed in buffer (1% wt/vol bovine serum albumin in phosphate-buffered saline, used for all subsequent washing and staining steps), were physically disrupted using sterile pipette tips, and were homogenized by repeated pipetting using wide-bore pipette tips. Stool suspensions were spun at 50 g for 1 min to pellet nonbacterial food particles. The supernatant was collected and passed through a 40-µm filter, and washed by centrifugation at 8,000 rcf for 3 min (same speed and time for subsequent washes). OD_{600} readings were taken of each suspension for normalization of input samples. Samples were stained with SYTO62 (1:500 dilution; Invitrogen) and anti-IgA (PE, clone: 11-44-2, dilution 1:40; eBioscience). All stains were performed for 15 min at 4°C. Stains were simultaneously performed using isotype control antibodies conjugated to PE, which yielded minimal to no staining for all experiments. Samples were then subjected to magnetic column–based separation using anti-PE microbeads (#130-048-801; Miltenyi) at a concentration of 1:20, and subsequent steps were followed as per the manufacturer protocol, and the IgA eluate was collected and spun by centrifugation to remove excess buffer prior to freezing. The IgA^+ fraction was then subjected to additional column enrichment. The column used for the first enrichment was washed by passing ethanol through the column with a plunger followed by PBS, and the IgA^+ sample was then applied and the manufacturer protocol was again performed. The final IgA+ fraction was centrifuged, and after removing excess buffer, it was frozen for downstream DNA extraction and 16S rRNA sequencing.

IgA-seq was performed on human stool in a similar fashion as described above and previously (Vujkovic-Cvijin et al., 2022), with the exception of using anti-human IgA PE (#130-093-128, 1:40 dilution; Miltenyi) for staining.

IgA-seq analysis

For murine IgA-seq, samples were subjected to rarefaction at 40,000 reads per sample, and for human IgA-seq, rarefaction at 30,000 reads per sample was performed. Dada2 was performed to generate ASV tables, and taxonomy was assigned using the RDP 18 database and the dada2 naïve Bayes classifier. For genus- and family-level analyses, ASVs were binned at the genus and family levels, respectively. Taxa with prevalence in <10% of samples were filtered out. IgA scores for each taxon were calculated by log10-transforming read counts and subtracting abundance of the IgA-enriched fraction from that of the IgA-depleted fraction.

For comparing human IgA scores between pRD and controls, linear mixed-effects models were used to control for age, sex, and country of residence with sex and country of residence considered random effects. For mouse IgA score comparisons between mutant and wild-type mice, Mann–Whitney U tests were performed.

Metabolomics analysis

Metabolite and lipid sample preparation

For all liquid chromatography–mass spectrometry (LCMS) methods, LCMS grade solvents were used. All samples were immersed in 0.4 ml of ice-cold methanol. To each sample, 0.4 ml of water and 0.4 ml of chloroform were added. Samples were shaken for 20 min under refrigeration and centrifuged at 16,000 *g* for 20 min 400 µl of each of the top (aqueous) layer was collected. A subaliquot of the aqueous layer was taken for O-benzylhydroxylamine (O-BHA) derivatization of carboxylic acids and SCFA analysis. The remaining aqueous layer was diluted as necessary in 50% methanol in water for LCMS analysis of central polar metabolites.

SCFA derivatization

Samples were derivatized with O-BHA according to previously established protocols (Jaochico et al., 2019; Zeng and Cao, 2018). Reaction buffer was prepared fresh consisting of 1 M pyridine and 0.5 M hydrochloric acid in water. A 35 µl aliquot of the aqueous extract was taken and to the sample was added 10 µl of 1 M O-BHA in reaction buffer and 10 µl of 1 M 1-ethyl-3-(3-dimethylaminopropyl)carbodiimide in reaction buffer. Samples were shaken at room temperature for 2 h. Each sample was quenched with 50 µl of 0.1% formic acid for 10 min. Derivatized carboxylic acid compounds were extracted with the addition of 400 µl ethyl acetate. Samples were centrifuged at 16k *g* for 10 min at 21°C to induce layering, and 200 µl of the upper (organic) layer was collected. The extract was dried under vacuum, and each sample was resuspended in 200 µl of water for LCMS injection.

LCMS

Tributylamine and all synthetic molecular references were purchased from MilliporeSigma. LCMS grade water, methanol, isopropanol, and acetic acid were purchased through Thermo Fisher Scientific.

Aqueous metabolites were analyzed using a combination of two analytical methods with opposing ionization polarities (Groveman et al., 2023; McCloskey et al., 2015). Both methodologies utilized an LD40 XR UHPLC (Shimadzu Co.) system for separation. Negative mode metabolites were detected using a 5,500 QTrap, and positive mode metabolites were detected with a 6,500+ QTrap mass spectrometer (AB Sciex Pte. Ltd.). Negative mode samples were separated on a Waters Atlantis T3 column (100 Å, 3 µm, 3 × 100 mm) and eluted using a binary gradient from 5 mM tributylamine, 5 mM acetic acid in 2% isopropanol, 5% methanol, 93% water (vol/vol) to 100% isopropanol over 5 min. Two distinct multiple reaction monitoring (MRM) pairs in negative mode were used for each metabolite. Positive mode method samples were separated across a Phenomenex Kinetex F5 column (100 Å, 2.6 µm, 100 × 2.1 mm) and eluted with a gradient from 0.1% formic acid in water to 0.1% formic acid in acetonitrile over 5 min.

Derivatized SCFA samples were analyzed using an LD40 XR UHPLC (Shimadzu Co.) system for separation and a 6,500+ QTrap mass spectrometer (AB Sciex Pte. Ltd.) for detection. Samples were separated with a Waters Atlantis dC18 column (100 Å, 3 µm, 3 × 100 mm) using a 6-min gradient from 5 to 80 B with buffer A consisting of 0.1% formic acid in water and B consisting of 0.1% formic acid in methanol. SCFAs and central metabolic carboxylic acids were detected using positive mode MRMs from previously established methods, and identity was confirmed by comparison with derivatized standards (Jaochico et al., 2019; Zeng and Cao, 2018).

All signals were integrated using Sciex OS 3.1 (AB Sciex Pte. Ltd.). Signals with >50% missing values for a specific tissue set were discarded, and remaining missing values were replaced with the lowest registered signal value. Where appropriate, signals with a quality control coefficient of variance >30% were discarded. Metabolites or lipids with multiple MRMs were quantified with the higher signal-to-noise MRM. Filtered datasets of the negative mode aqueous metabolites and the bulk lipidomics were total sum-normalized after initial filtering. The SCFA dataset and the positive mode aqueous metabolomics dataset were scaled and combined with the negative mode aqueous metabolite dataset using common signal for citrate and serine, respectively. A Benjamini–Hochberg method for correction for multiple comparisons was imposed where indicated.

Online supplemental material

Fig. S1 shows mean recombination activity of mutant RAG alleles and colonic inflammation in pRD. Fig. S2 shows characterization of colonic and systemic inflammation in *Rag1*$^{w/w}$ (W/W) mice. Fig. S3 shows scRNA-seq of LP CD4^{+} T cells in W/W and wild-type mice. Fig. S4 shows composition and diversity of fecal microbiota in W/W and wild-type mice. Fig. S5 shows effects of various treatment modalities on intestinal and systemic inflammation, and on TCR repertoire composition.

Data availability

The mRNA, VDJ (TCR), and HTO sequencing data underlying Figs. 3, 5, 6, S3, and S5 have been deposited on GEO under the accession number GSE277151, whereas the analysis code and scripts are available on https://github.com/cihangenome/immunological-microbial-signatures-RAG-deficiency. The raw microbiome sequence and IgA-seq data underlying Figs. 4, 6, 7, and S4 have been deposited in NCBI's Sequencing Read Archive database under the Bioproject number PRJNA1159340 (https://www.ncbi.nlm.nih.gov/bioproject/PRJNA1159340/).

Acknowledgments

The authors thank Sean P. Conlan and Clayton Deming from the Microbial Genomics Section, Translational and Functional Genomics Branch, National Human Genome Research Institute, National Institutes of Health, Bethesda, MD, USA, for their support in the microbiota characterization of the mouse model.

This work was supported by the Division of Intramural Research of the National Institute of Allergy and Infectious Diseases (NIAID), National Institutes of Health (NIH) (grant AI001222 to L.D. Notarangelo). This project has been funded in part with Federal funds from the NIAID, NIH, Department of Health and Human Services under Bioinformatics and Computational Biosciences Branch Support Services Contract HHSN316201300006W/75N93022F00001 to Guidehouse Digital. R. Castagnoli developed part of this project while being a participant in the U.S. National Institutes of Health (NIH) Graduate Partnership Program. R. Castagnoli has been awarded the Fellowship "Progressi in Biologia e Medicina" from Fondazione Ghislieri, Collegio Ghislieri, Pavia, Italy, to support the investigation on microbiota–host interactions in inborn errors of immunity. I. Vujkovic-Cvijin was supported by NHLBI, NIH (grant DP1HL174182), NIDDK, NIH (grant U01DK062413), the Crohn's & Colitis Foundation Career Development Award #831262, and the F. Widjaja Inflammatory Bowel Disease Institute of Cedars-Sinai Medical Center.

Author contributions: R. Castagnoli: conceptualization, data curation, formal analysis, investigation, methodology, project administration, validation, visualization, and writing—original draft, review, and editing. F. Pala: conceptualization, data curation, formal analysis, investigation, methodology, validation, visualization, and writing—original draft, review, and editing. P. Subramanian: data curation, formal analysis, methodology, software, validation, visualization, and writing—original draft, review, and editing. C. Oguz: data curation, formal analysis, software, and writing—original draft, review, and editing. B. Schwarz: data curation, formal analysis, investigation, methodology, resources, and visualization. A.I. Lim: investigation. A.S. Burns: investigation, resources, validation, and writing—review and editing. E. Fontana: investigation. M. Bosticardo: investigation and writing—review and editing. C. Corsino: investigation and project administration. A. Angelova: formal analysis. O.M. Delmonte: resources. H. Kenney: investigation, project administration, and resources. D. Riley: investigation and writing—review and editing. G. Smith: investigation, methodology, resources, and writing—review and editing. L. Ott de Bruin: writing—review and editing. V. Oikonomou: investigation. L. Dos Santos Dias: investigation and writing—review and editing. D. Fink: investigation. E. Bohrnsen: conceptualization, data curation, formal analysis, and writing—review and editing.

C.D. Kimzey: formal analysis and investigation. G.L. Marseglia: resources. G. Alva-Lozada: resources. J.R.E. Bergerson: resources and writing—review and editing. A. Brett: resources. K.W. Brigatti: investigation, project administration, and resources. D. Dimitrova: resources. C.M. Dutmer: investigation, resources, and writing—review and editing. A.F. Freeman: resources, and writing—review and editing. H. Ale: resources. S.M. Holland: funding acquisition, investigation, and resources. F. Licciardi: investigation. S. Pasic: resources. L.E. Poskitt: data curation. D.E. Potts: data curation, investigation, and writing—review and editing. J.F. Dasso: resources and writing—review and editing. S.O. Sharapova: resources. K.A. Strauss: conceptualization, data curation, project administration, resources, supervision, and writing—review and editing. B.R. Ward: resources. M. Yilmaz: resources. D.B. Kuhns: formal analysis, investigation, and resources. M.S. Lionakis: funding acquisition, investigation, supervision, and writing—review and editing. S.R. Daley: formal analysis and software. H.H. Kong: conceptualization, investigation, resources, and writing—review and editing. J.A. Segre: methodology and writing—review and editing. A. Villa: conceptualization. S. Pittaluga: resources and visualization. J.E. Walter: data curation, funding acquisition, resources, and writing—original draft, review, and editing. I. Vujkovic-Cvijin: formal analysis, investigation, methodology, software, validation, visualization, and writing—review and editing. Y. Belkaid: conceptualization, investigation, resources, and supervision. L.D. Notarangelo: conceptualization, funding acquisition, investigation, methodology, project administration, resources, supervision, validation, and writing—original draft, review, and editing.

Disclosures: B.R. Ward reported grants from Swedish Orphan Biovitrum, Astra Zeneca, and Blueprint Medicines, and personal fees from Carilion Services outside the submitted work. S.R. Daley reported grants from Resseptor Therapeutics Ltd. and personal fees from Resseptor Therapeutics Ltd. outside the submitted work. No other disclosures were reported.

Submitted: 26 October 2024
Revised: 16 March 2025
Accepted: 10 April 2025

References

Abdel-Gadir, A., E. Stephen-Victor, G.K. Gerber, M. Noval Rivas, S. Wang, H. Harb, L. Wang, N. Li, E. Crestani, S. Spielman, et al. 2019. Microbiota therapy acts via a regulatory T cell MyD88/RORγt pathway to suppress food allergy. *Nat. Med.* 25:1164–1174. https://doi.org/10.1038/s41591-019-0461-z

Al Nabhani, Z., S. Dulauroy, R. Marques, C. Cousu, S. Al Bounny, F. Déjardin, T. Sparwasser, M. Bérard, N. Cerf-Bensussan, and G. Eberl. 2019. A weaning reaction to microbiota is required for resistance to immunopathologies in the adult. *Immunity*. 50:1276–1288.e5. https://doi.org/10.1016/j.immuni.2019.02.014

Al-Hebshi, N.N., A.T. Nasher, A.M. Idris, and T. Chen. 2015. Robust species taxonomy assignment algorithm for 16S rRNA NGS reads: Application to oral carcinoma samples. *J. Oral Microbiol.* 7:28934. https://doi.org/10.3402/jom.v7.28934

Annunziato, F., L. Cosmi, V. Santarlasci, L. Maggi, F. Liotta, B. Mazzinghi, E. Parente, L. Filì, S. Ferri, F. Frosali, et al. 2007. Phenotypic and functional features of human Th17 cells. *J. Exp. Med.* 204:1849–1861. https://doi.org/10.1084/jem.20070663

Ansaldo, E., T.K. Farley, and Y. Belkaid. 2021. Control of immunity by the microbiota. *Annu. Rev. Immunol.* 39:449–479. https://doi.org/10.1146/annurev-immunol-093019-112348

Aranda, R., B.C. Sydora, P.L. McAllister, S.W. Binder, H.Y. Yang, S.R. Targan, and M. Kronenberg. 1997. Analysis of intestinal lymphocytes in mouse colitis mediated by transfer of CD4$^+$, CD45RBhigh T cells to SCID recipients. *J. Immunol.* 158:3464–3473. https://doi.org/10.4049/jimmunol.158.7.3464

Arpaia, N., C. Campbell, X. Fan, S. Dikiy, J. van der Veeken, P. deRoos, H. Liu, J.R. Cross, K. Pfeffer, P.J. Coffer, and A.Y. Rudensky. 2013. Metabolites produced by commensal bacteria promote peripheral regulatory T-cell generation. *Nature*. 504:451–455. https://doi.org/10.1038/nature12726

Atarashi, K., W. Suda, C. Luo, T. Kawaguchi, I. Motoo, S. Narushima, Y. Kiguchi, K. Yasuma, E. Watanabe, T. Tanoue, et al. 2017. Ectopic colonization of oral bacteria in the intestine drives T_H1 cell induction and inflammation. *Science*. 358:359–365. https://doi.org/10.1126/science.aan4526

Borcherding, N., A. Vishwakarma, A.P. Voigt, A. Bellizzi, J. Kaplan, K. Nepple, A.K. Salem, R.W. Jenkins, Y. Zakharia, and W. Zhang. 2021. Mapping the immune environment in clear cell renal carcinoma by single-cell genomics. *Commun. Biol.* 4:122. https://doi.org/10.1038/s42003-020-01625-6

Bosticardo, M., K. Dobbs, O.M. Delmonte, A.J. Martins, F. Pala, T. Kawai, H. Kenney, G. Magro, L.B. Rosen, Y. Yamazaki, et al. 2025. Multiomics dissection of human RAG deficiency reveals distinctive patterns of immune dysregulation but a common inflammatory signature. *Sci. Immunol.* 10:eadq1697. https://doi.org/10.1126/sciimmunol.adq1697

Callahan, B.J., P.J. McMurdie, M.J. Rosen, A.W. Han, A.J. Johnson, and S.P. Holmes. 2016. DADA2: High-resolution sample inference from Illumina amplicon data. *Nat. Methods*. 13:581–583. https://doi.org/10.1038/nmeth.3869

Cao, H., J. Diao, H. Liu, S. Liu, J. Liu, J. Yuan, and J. Lin. 2023. The pathogenicity and synergistic action of Th1 and Th17 cells in inflammatory bowel diseases. *Inflamm. Bowel Dis.* 29:818–829. https://doi.org/10.1093/ibd/izac199

Csomos, K., B. Ujhazi, P. Blazso, J.L. Herrera, C.M. Tipton, T. Kawai, S. Gordon, M. Ellison, K. Wu, M. Stowell, et al. 2022. Partial RAG deficiency in humans induces dysregulated peripheral lymphocyte development and humoral tolerance defect with accumulation of T-bet$^+$ B cells. *Nat. Immunol.* 23:1256–1272. https://doi.org/10.1038/s41590-022-01271-6

Daley, S.R., H.F. Koay, K. Dobbs, M. Bosticardo, R.C. Wirasinha, F. Pala, R. Castagnoli, J.H. Rowe, L.M. Ott de Bruin, S. Keles, et al. 2019. Cysteine and hydrophobic residues in CDR3 serve as distinct T-cell self-reactivity indices. *J. Allergy Clin. Immunol.* 144:333–336. https://doi.org/10.1016/j.jaci.2019.03.022

Deleu, S., K. Machiels, J. Raes, K. Verbeke, and S. Vermeire. 2021. Short chain fatty acids and its producing organisms: An overlooked therapy for IBD? *EBioMedicine*. 66:103293. https://doi.org/10.1016/j.ebiom.2021.103293

Delmonte, O.M., A. Villa, and L.D. Notarangelo. 2020. Immune dysregulation in patients with RAG deficiency and other forms of combined immune deficiency. *Blood*. 135:610–619. https://doi.org/10.1182/blood.2019000923

Dikiy, S., A.P. Ghelani, A.G. Levine, S. Martis, P. Giovanelli, Z.M. Wang, G. Beroshvili, Y. Pritykin, C. Krishna, X. Huang, et al. 2025. Terminal differentiation and persistence of effector regulatory T cells essential for preventing intestinal inflammation. *Nat. Immunol.* 26:444–458. https://doi.org/10.1038/s41590-024-02075-6

Donaldson, G.P., M.S. Ladinsky, K.B. Yu, J.G. Sanders, B.B. Yoo, W.C. Chou, M.E. Conner, A.M. Earl, R. Knight, P.J. Bjorkman, and S.K. Mazmanian. 2018. Gut microbiota utilize immunoglobulin A for mucosal colonization. *Science*. 360:795–800. https://doi.org/10.1126/science.aaq0926

Douglas, G.M., V.J. Maffei, J.R. Zaneveld, S.N. Yurgel, J.R. Brown, C.M. Taylor, C. Huttenhower, and M.G.I. Langille. 2020. PICRUSt2 for prediction of metagenome functions. *Nat. Biotechnol.* 38:685–688. https://doi.org/10.1038/s41587-020-0548-6

Fan, Y., and O. Pedersen. 2021. Gut microbiota in human metabolic health and disease. *Nat. Rev. Microbiol.* 19:55–71. https://doi.org/10.1038/s41579-020-0433-9

Finak, G., A. McDavid, M. Yajima, J. Deng, V. Gersuk, A.K. Shalek, C.K. Slichter, H.W. Miller, M.J. McElrath, M. Prlic, et al. 2015. MAST: A flexible statistical framework for assessing transcriptional changes and characterizing heterogeneity in single-cell RNA sequencing data. *Genome Biol.* 16:278. https://doi.org/10.1186/s13059-015-0844-5

Fontenot, J.D., M.A. Gavin, and A.Y. Rudensky. 2003. Foxp3 programs the development and function of CD4$^+$CD25$^+$ regulatory T cells. *Nat. Immunol.* 4:330–336. https://doi.org/10.1038/ni904

Fugmann, S.D., A.I. Lee, P.E. Shockett, I.J. Villey, and D.G. Schatz. 2000. The RAG proteins and V(D)J recombination: Complexes, ends, and transposition. *Annu. Rev. Immunol.* 18:495–527. https://doi.org/10.1146/annurev.immunol.18.1.495

Furusawa, Y., Y. Obata, S. Fukuda, T.A. Endo, G. Nakato, D. Takahashi, Y. Nakanishi, C. Uetake, K. Kato, T. Kato, et al. 2013. Commensal microbe-derived butyrate induces the differentiation of colonic regulatory T cells. *Nature*. 504:446–450. https://doi.org/10.1038/nature12721

Fusco, W., M.B. Lorenzo, M. Cintoni, S. Porcari, E. Rinninella, F. Kaitsas, E. Lener, M.C. Mele, A. Gasbarrini, M.C. Collado, et al. 2023. Short-chain fatty-acid-producing bacteria: Key components of the human gut microbiota. *Nutrients*. 15:2211. https://doi.org/10.3390/nu15092211

Gilbert, J.A., M.J. Blaser, J.G. Caporaso, J.K. Jansson, S.V. Lynch, and R. Knight. 2018. Current understanding of the human microbiome. *Nat. Med.* 24:392–400. https://doi.org/10.1038/nm.4517

Groveman, B.R., B. Schwarz, E. Bohrnsen, S.T. Foliaki, J.A. Carroll, A.R. Wood, C.M. Bosio, and C.L. Haigh. 2023. A PrP EGFR signaling axis controls neural stem cell senescence through modulating cellular energy pathways. *J. Biol. Chem.* 299:105319. https://doi.org/10.1016/j.jbc.2023.105319

Gu, Y., R. Bartolomé-Casado, C. Xu, A. Bertocchi, A. Janney, C. Heuberger, C.F. Pearson, S.A. Teichmann, E.E. Thornton, and F. Powrie. 2024. Immune microniches shape intestinal T_{reg} function. *Nature*. 628:854–862. https://doi.org/10.1038/s41586-024-07251-0

Hao, Y., S. Hao, E. Andersen-Nissen, W.M. Mauck III, S. Zheng, A. Butler, M.J. Lee, A.J. Wilk, C. Darby, M. Zager, et al. 2021. Integrated analysis of multimodal single-cell data. *Cell*. 184:3573–3587.e29. https://doi.org/10.1016/j.cell.2021.04.048

Hooper, L.V., and A.J. Macpherson. 2010. Immune adaptations that maintain homeostasis with the intestinal microbiota. *Nat. Rev. Immunol.* 10:159–169. https://doi.org/10.1038/nri2710

Ivanov, I.I., T. Tuganbaev, A.N. Skelly, and K. Honda. 2022. T cell responses to the microbiota. *Annu. Rev. Immunol.* 40:559–587. https://doi.org/10.1146/annurev-immunol-101320-011829

Jaochico, A., D. Sangaraju, and S.K. Shahidi-Latham. 2019. A rapid derivatization based LC-MS/MS method for quantitation of short chain fatty acids in human plasma and urine. *Bioanalysis*. 11:741–753. https://doi.org/10.4155/bio-2018-0241

Joseph, S., J. Aduse-Opoku, A. Hashim, E. Hanski, R. Streich, S.C.L. Knowles, A.B. Pedersen, W.G. Wade, and M.A. Curtis. 2021. A 16S rRNA gene and draft genome database for the murine oral bacterial community. *mSystems*. 6:e01222-20. https://doi.org/10.1128/mSystems.01222-20

Kitamoto, S., H. Nagao-Kitamoto, Y. Jiao, M.G. Gillilland, 3rd, A. Hayashi, J. Imai, K. Sugihara, M. Miyoshi, J.C. Brazil, P. Kuffa, et al. 2020. The intermucosal connection between the mouth and gut in commensal pathobiont-driven colitis. *Cell*. 182:447–462.e14. https://doi.org/10.1016/j.cell.2020.05.048

Kozich, J.J., S.L. Westcott, N.T. Baxter, S.K. Highlander, and P.D. Schloss. 2013. Development of a dual-index sequencing strategy and curation pipeline for analyzing amplicon sequence data on the MiSeq Illumina sequencing platform. *Appl. Environ. Microbiol.* 79:5112–5120. https://doi.org/10.1128/AEM.01043-13

Kurmaeva, E., J.D. Lord, S. Zhang, J.R. Bao, C.G. Kevil, M.B. Grisham, and D.V. Ostanin. 2014. T cell-associated α4β7 but not α4β1 integrin is required for the induction and perpetuation of chronic colitis. *Mucosal Immunol.* 7:1354–1365. https://doi.org/10.1038/mi.2014.22

Kuznetsova, A., P.B. Brockhoff, and R.H.B. Christensen. 2017. lmerTest package: Tests in linear mixed effects models. *J. Stat. Softw.* 82. https://doi.org/10.18637/jss.v082.i13

Langille, M.G., J. Zaneveld, J.G. Caporaso, D. McDonald, D. Knights, J.A. Reyes, J.C. Clemente, D.E. Burkepile, R.L. Vega Thurber, R. Knight, et al. 2013. Predictive functional profiling of microbial communities using 16S rRNA marker gene sequences. *Nat. Biotechnol.* 31:814–821. https://doi.org/10.1038/nbt.2676

Lee, Y.N., F. Frugoni, K. Dobbs, I. Tirosh, L. Du, F.A. Ververs, H. Ru, L. Ott de Bruin, M. Adeli, J.H. Bleesing, et al. 2016. Characterization of T and B cell repertoire diversity in patients with RAG deficiency. *Sci. Immunol.* 1:eaah6109. https://doi.org/10.1126/sciimmunol.aah6109

Liao, Y., J. Wang, E.J. Jaehnig, Z. Shi, and B. Zhang. 2019. WebGestalt 2019: Gene set analysis toolkit with revamped UIs and APIs. *Nucleic Acids Res.* 47:W199–W205. https://doi.org/10.1093/nar/gkz401

Lindebo Holm, T., S.S. Poulsen, H. Markholst, and S. Reedtz-Runge. 2012. Pharmacological evaluation of the SCID T cell transfer model of colitis: As a model of Crohn's disease. *Int. J. Inflamm.* 2012:412178. https://doi.org/10.1155/2012/412178

Lubin, J.B., J. Green, S. Maddux, L. Denu, T. Duranova, M. Lanza, M. Wynosky-Dolfi, J.N. Flores, L.P. Grimes, I.E. Brodsky, et al. 2023. Arresting microbiome development limits immune system maturation and resistance to infection in mice. *Cell Host Microbe*. 31:554–570.e7. https://doi.org/10.1016/j.chom.2023.03.006

Lui, V.G., M. Hoenig, B. Cabrera-Martinez, R.M. Baxter, J.E. Garcia-Perez, O. Bailey, A. Acharya, K. Lundquist, J. Capera, P. Matusewicz, et al. 2024. A partial human LCK defect causes a T cell immunodeficiency with intestinal inflammation. *J. Exp. Med.* 221:e20230927. https://doi.org/10.1084/jem.20230927

Lund, P.J., L.A. Gates, M. Leboeuf, S.A. Smith, L. Chau, M. Lopes, E.S. Friedman, Y. Saiman, M.S. Kim, C.A. Shoffler, et al. 2022. Stable isotope tracing in vivo reveals a metabolic bridge linking the microbiota to host histone acetylation. *Cell Rep.* 41:111809. https://doi.org/10.1016/j.celrep.2022.111809

Ma, S. 2025. MMUPHin: Meta-analysis methods with uniform pipeline for heterogeneity in microbiome studies. *Bioconductor*. https://doi.org/10.18129/B9.bioc.MMUPHin

Mallick, H., A. Rahnavard, L.J. McIver, S. Ma, Y. Zhang, L.H. Nguyen, T.L. Tickle, G. Weingart, B. Ren, E.H. Schwager, et al. 2021. Multivariable association discovery in population-scale meta-omics studies. *PLoS Comput. Biol.* 17:e1009442. https://doi.org/10.1371/journal.pcbi.1009442

Mann, E.R., Y.K. Lam, and H.H. Uhlig. 2024. Short-chain fatty acids: Linking diet, the microbiome and immunity. *Nat. Rev. Immunol.* 24:577–595. https://doi.org/10.1038/s41577-024-01014-8

McCloskey, D., J.A. Gangoiti, B.O. Palsson, and A.M. Feist. 2015. A pH and solvent optimized reverse-phase ion-paring-LC–MS/MS method that leverages multiple scan-types for targeted absolute quantification of intracellular metabolites. *Metabolomics*. 11:1338–1350. https://doi.org/10.1007/s11306-015-0790-y

Murai, M., O. Turovskaya, G. Kim, R. Madan, C.L. Karp, H. Cheroutre, and M. Kronenberg. 2009. Interleukin 10 acts on regulatory T cells to maintain expression of the transcription factor Foxp3 and suppressive function in mice with colitis. *Nat. Immunol.* 10:1178–1184. https://doi.org/10.1038/ni.1791

Nguyen, T.L., S. Vieira-Silva, A. Liston, and J. Raes. 2015. How informative is the mouse for human gut microbiota research? *Dis. Model. Mech.* 8:1–16. https://doi.org/10.1242/dmm.017400

Ohnmacht, C., J.H. Park, S. Cording, J.B. Wing, K. Atarashi, Y. Obata, V. Gaboriau-Routhiau, R. Marques, S. Dulauroy, M. Fedoseeva, et al. 2015. MUCOSAL IMMUNOLOGY. The microbiota regulates type 2 immunity through RORγt$^+$ T cells. *Science*. 349:989–993. https://doi.org/10.1126/science.aac4263

Ott de Bruin, L., W. Yang, K. Capuder, Y.N. Lee, M. Antolini, R. Meyers, M. Gellert, K. Musunuru, J. Manis, and L. Notarangelo. 2016. Rapid generation of novel models of RAG1 deficiency by CRISPR/Cas9-induced mutagenesis in murine zygotes. *Oncotarget*. 7:12962–12974. https://doi.org/10.18632/oncotarget.7341

Ott de Bruin, L.M., M. Bosticardo, A. Barbieri, S.G. Lin, J.H. Rowe, P.L. Poliani, K. Ching, D. Eriksson, N. Landegren, O. Kämpe, et al. 2018. Hypomorphic Rag1 mutations alter the preimmune repertoire at early stages of lymphoid development. *Blood*. 132:281–292. https://doi.org/10.1182/blood-2017-12-820985

Ott, S.J., M. Musfeldt, D.F. Wenderoth, J. Hampe, O. Brant, U.R. Fölsch, K.N. Timmis, and S. Schreiber. 2004. Reduction in diversity of the colonic mucosa associated bacterial microflora in patients with active inflammatory bowel disease. *Gut*. 53:685–693. https://doi.org/10.1136/gut.2003.025403

Pabst, O., and E. Slack. 2020. IgA and the intestinal microbiota: The importance of being specific. *Mucosal Immunol.* 13:12–21. https://doi.org/10.1038/s41385-019-0227-4

Quast, C., E. Pruesse, P. Yilmaz, J. Gerken, T. Schweer, P. Yarza, J. Peplies, and F.O. Glöckner. 2013. The SILVA ribosomal RNA gene database project: Improved data processing and web-based tools. *Nucleic Acids Res.* 41:D590–D596. https://doi.org/10.1093/nar/gks1219

Read, E., M.A. Curtis, and J.F. Neves. 2021. The role of oral bacteria in inflammatory bowel disease. *Nat. Rev. Gastroenterol. Hepatol.* 18:731–742. https://doi.org/10.1038/s41575-021-00488-4

Reinoso Webb, C., H. den Bakker, I. Koboziev, Y. Jones-Hall, K. Rao Kottapalli, D. Ostanin, K.L. Furr, Q. Mu, X.M. Luo, and M.B. Grisham. 2018. Differential susceptibility to T cell-induced colitis in mice: Role of the intestinal microbiota. *Inflamm. Bowel Dis.* 24:361–379. https://doi.org/10.1093/ibd/izx014

Rigoni, R., E. Fontana, K. Dobbs, V. Marrella, V. Taverniti, V. Maina, A. Facoetti, G. D'Amico, W. Al-Herz, M.E. Cruz-Munoz, et al. 2020.

Cutaneous barrier leakage and gut inflammation drive skin disease in Omenn syndrome. *J. Allergy Clin. Immunol.* 146:1165–1179.e11. https://doi.org/10.1016/j.jaci.2020.04.005

Rigoni, R., E. Fontana, S. Guglielmetti, B. Fosso, A.M. D'Erchia, V. Maina, V. Taverniti, M.C. Castiello, S. Mantero, G. Pacchiana, et al. 2016. Intestinal microbiota sustains inflammation and autoimmunity induced by hypomorphic RAG defects. *J. Exp. Med.* 213:355–375. https://doi.org/10.1084/jem.20151116

Robertson, S.J., P. Lemire, H. Maughan, A. Goethel, W. Turpin, L. Bedrani, D.S. Guttman, K. Croitoru, S.E. Girardin, and D.J. Philpott. 2019. Comparison of Co-housing and littermate methods for microbiota standardization in mouse models. *Cell Rep.* 27:1910–1919.e2. https://doi.org/10.1016/j.celrep.2019.04.023

Rook, G., F. Bäckhed, B.R. Levin, M.J. McFall-Ngai, and A.R. McLean. 2017. Evolution, human-microbe interactions, and life history plasticity. *Lancet*. 390:521–530. https://doi.org/10.1016/S0140-6736(17)30566-4

Rosser, E.C., K. Oleinika, S. Tonon, R. Doyle, A. Bosma, N.A. Carter, K.A. Harris, S.A. Jones, N. Klein, and C. Mauri. 2014. Regulatory B cells are induced by gut microbiota-driven interleukin-1β and interleukin-6 production. *Nat. Med.* 20:1334–1339. https://doi.org/10.1038/nm.3680

Rowe, J.H., B.D. Stadinski, L.A. Henderson, L. Ott de Bruin, O. Delmonte, Y.N. Lee, M.T. de la Morena, R.K. Goyal, A. Hayward, C.H. Huang, et al. 2017. Abnormalities of T-cell receptor repertoire in CD4(+) regulatory and conventional T cells in patients with RAG mutations: Implications for autoimmunity. *J. Allergy Clin. Immunol.* 140:1739–1743.e7. https://doi.org/10.1016/j.jaci.2017.08.001

Sacco, K., R. Castagnoli, S. Vakkilainen, C. Liu, O.M. Delmonte, C. Oguz, I.M. Kaplan, S. Alehashemi, P.D. Burbelo, F. Bhuyan, et al. 2022. Immunopathological signatures in multisystem inflammatory syndrome in children and pediatric COVID-19. *Nat. Med.* 28:1050–1062. https://doi.org/10.1038/s41591-022-01724-3

Schuetz, C., J. Gerke, M. Ege, J. Walter, M. Kusters, A. Worth, J.A. Kanakry, D. Dimitrova, B. Wolska-Kuśnierz, K. Chen, et al. 2023. Hypomorphic RAG deficiency: Impact of disease burden on survival and thymic recovery argues for early diagnosis and HSCT. *Blood*. 141:713–724. https://doi.org/10.1182/blood.2022017667

Schwarz, K., G.H. Gauss, L. Ludwig, U. Pannicke, Z. Li, D. Lindner, W. Friedrich, R.A. Seger, T.E. Hansen-Hagge, S. Desiderio, et al. 1996. RAG mutations in human B cell-negative SCID. *Science*. 274:97–99. https://doi.org/10.1126/science.274.5284.97

Sefik, E., N. Geva-Zatorsky, S. Oh, L. Konnikova, D. Zemmour, A.M. McGuire, D. Burzyn, A. Ortiz-Lopez, M. Lobera, J. Yang, et al. 2015. MUCOSAL IMMUNOLOGY. Individual intestinal symbionts induce a distinct population of RORγ$^+$ regulatory T cells. *Science*. 349:993–997. https://doi.org/10.1126/science.aaa9420

Sheridan, B.S., Q.M. Pham, Y.T. Lee, L.S. Cauley, L. Puddington, and L. Lefrançois. 2014. Oral infection drives a distinct population of intestinal resident memory CD8(+) T cells with enhanced protective function. *Immunity*. 40:747–757. https://doi.org/10.1016/j.immuni.2014.03.007

Sim, C.K., S.S. Kashaf, A. Stacy, D.M. Proctor, A. Almeida, N. Bouladoux, M. Chen, R.D. Finn, Y. Belkaid, S. Conlan, et al. 2022. A mouse model of occult intestinal colonization demonstrating antibiotic-induced outgrowth of carbapenem-resistant Enterobacteriaceae. *Microbiome*. 10:43. https://doi.org/10.1186/s40168-021-01207-6

Singh, K., M. Hjort, L. Thorvaldson, and S. Sandler. 2015. Concomitant analysis of Helios and Neuropilin-1 as a marker to detect thymic derived regulatory T cells in naïve mice. *Sci. Rep.* 5:7767. https://doi.org/10.1038/srep07767

Smith, P.M., M.R. Howitt, N. Panikov, M. Michaud, C.A. Gallini, M. Bohlooly-Y, J.N. Glickman, and W.S. Garrett. 2013. The microbial metabolites, short-chain fatty acids, regulate colonic Treg cell homeostasis. *Science*. 341:569–573. https://doi.org/10.1126/science.1241165

Stadinski, B.D., K. Shekhar, I. Gómez-Touriño, J. Jung, K. Sasaki, A.K. Sewell, M. Peakman, A.K. Chakraborty, and E.S. Huseby. 2016. Hydrophobic CDR3 residues promote the development of self-reactive T cells. *Nat. Immunol.* 17:946–955. https://doi.org/10.1038/ni.3491

Takeuchi, T., Y. Nakanishi, and H. Ohno. 2024. Microbial metabolites and gut immunology. *Annu. Rev. Immunol.* 42:153–178. https://doi.org/10.1146/annurev-immunol-090222-102035

Tan, J., C. McKenzie, P.J. Vuillermin, G. Goverse, C.G. Vinuesa, R.E. Mebius, L. Macia, and C.R. Mackay. 2016. Dietary fiber and bacterial SCFA enhance oral tolerance and protect against food allergy through diverse cellular pathways. *Cell Rep.* 15:2809–2824. https://doi.org/10.1016/j.celrep.2016.05.047

Thornton, A.M., P.E. Korty, D.Q. Tran, E.A. Wohlfert, P.E. Murray, Y. Belkaid, and E.M. Shevach. 2010. Expression of Helios, an Ikaros transcription factor family member, differentiates thymic-derived from peripherally induced Foxp3$^+$ T regulatory cells. *J. Immunol.* 184:3433–3441. https://doi.org/10.4049/jimmunol.0904028

Villa, A., S. Santagata, F. Bozzi, S. Giliani, A. Frattini, L. Imberti, L.B. Gatta, H.D. Ochs, K. Schwarz, L.D. Notarangelo, et al. 1998. Partial V(D)J recombination activity leads to Omenn syndrome. *Cell*. 93:885–896. https://doi.org/10.1016/S0092-8674(00)81448-8

Vujkovic-Cvijin, I., H.C. Welles, C.W.Y. Ha, L. Huq, S. Mistry, J.M. Brenchley, G. Trinchieri, S. Devkota, and Y. Belkaid. 2022. The systemic anti-microbiota IgG repertoire can identify gut bacteria that translocate across gut barrier surfaces. *Sci. Transl. Med.* 14:eabl3927. https://doi.org/10.1126/scitranslmed.abl3927

Wang, F., J. Flanagan, N. Su, L.C. Wang, S. Bui, A. Nielson, X. Wu, H.T. Vo, X.J. Ma, and Y. Luo. 2012. RNAscope: A novel in situ RNA analysis platform for formalin-fixed, paraffin-embedded tissues. *J. Mol. Diagn.* 14:22–29. https://doi.org/10.1016/j.jmoldx.2011.08.002

Wang, R.X., J.S. Lee, E.L. Campbell, and S.P. Colgan. 2020. Microbiota-derived butyrate dynamically regulates intestinal homeostasis through regulation of actin-associated protein synaptopodin. *Proc. Natl. Acad. Sci. USA*. 117:11648–11657. https://doi.org/10.1073/pnas.1917597117

Wickham, H. 2016. ggplot2: Elegant Graphics for Data Analysis. Second edition. Springer Cham, Cham, Switzerland. 260.

Wohlfert, E.A., J.R. Grainger, N. Bouladoux, J.E. Konkel, G. Oldenhove, C.H. Ribeiro, J.A. Hall, R. Yagi, S. Naik, R. Bhairavabhotla, et al. 2011. GATA3 controls Foxp3(+) regulatory T cell fate during inflammation in mice. *J. Clin. Invest.* 121:4503–4515. https://doi.org/10.1172/JCI57456

Wyant, T., E. Fedyk, and B. Abhyankar. 2016. An overview of the mechanism of action of the monoclonal antibody vedolizumab. *J. Crohns Colitis*. 10:1437–1444. https://doi.org/10.1093/ecco-jcc/jjw092

Xu, M., M. Pokrovskii, Y. Ding, R. Yi, C. Au, O.J. Harrison, C. Galan, Y. Belkaid, R. Bonneau, and D.R. Littman. 2018. c-MAF-dependent regulatory T cells mediate immunological tolerance to a gut pathobiont. *Nature*. 554:373–377. https://doi.org/10.1038/nature25500

Yang, Y., and N.W. Palm. 2020. Immunoglobulin A and the microbiome. *Curr. Opin. Microbiol.* 56:89–96. https://doi.org/10.1016/j.mib.2020.08.003

Zeng, M., and H. Cao. 2018. Fast quantification of short chain fatty acids and ketone bodies by liquid chromatography-tandem mass spectrometry after facile derivatization coupled with liquid-liquid extraction. *J. Chromatogr. B Analyt. Technol. Biomed. Life Sci.* 1083:137–145. https://doi.org/10.1016/j.jchromb.2018.02.040

Zheng, G.X., J.M. Terry, P. Belgrader, P. Ryvkin, Z.W. Bent, R. Wilson, S.B. Ziraldo, T.D. Wheeler, G.P. McDermott, J. Zhu, et al. 2017. Massively parallel digital transcriptional profiling of single cells. *Nat. Commun.* 8:14049. https://doi.org/10.1038/ncomms14049

Supplemental material

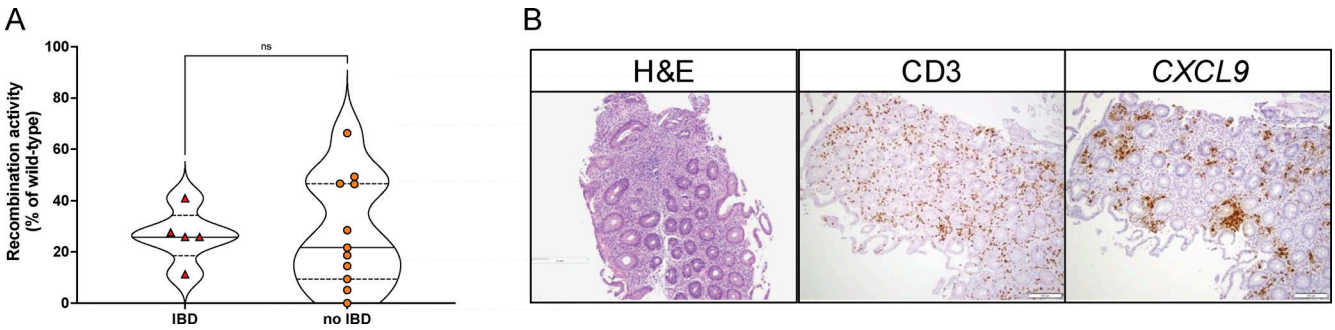

Figure S1. **Mean recombination activity of mutant RAG alleles and colonic inflammation in pRD. (A)** Recombination activity of variants in the cohort of pRD patients with (*n* = 5) and without IBD (*n* = 11). Statistical analysis was performed using a Mann–Whitney test. **(B)** Immunohistochemical analysis of colon biopsy isolated from P2, showing anti-CD3 staining and *CXCL9* transcript by in situ hybridization. All images are 10× magnification (scale bars: 100 µm).

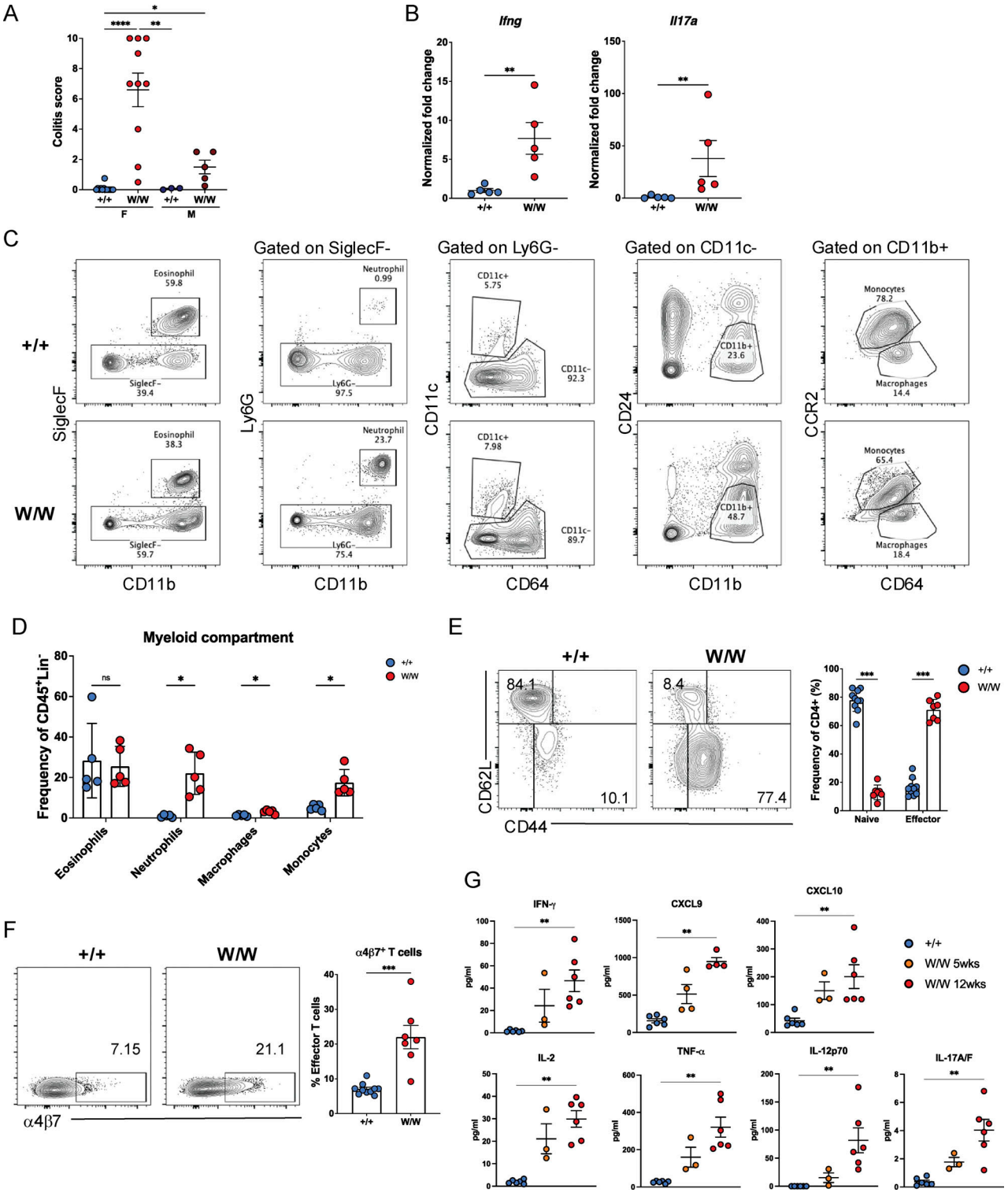

Figure S2. **Characterization of colonic and systemic inflammation in W/W mice. (A)** Colitis score based on immunohistochemical analysis of 12-wk-old (wo) wild-type (+/+) mice or *Rag1*$^{w/w}$ (W/W) mice split by sex (female, F; male, M; *n* = 5–10/group). Bars show the mean with SEM. Statistical analysis was performed using a Mann–Whitney test. **(B)** Gene expression from total large intestine lysate (*n* = 5/group). Statistical analysis was performed using a Mann–Whitney test. **(C and D)** Representative plot (C) and frequency (D) of myeloid cells isolated from the LP of 12wo +/+ mice or W/W mice (*n* = 5/group). Statistical analysis was performed using a Mann–Whitney test. **(E)** Representative plot and frequency of naïve ($CD62L^+CD44^-$) and effector ($CD62L^-CD44^+$) $CD4^+$ T cells isolated from MLN of 12wo +/+ mice (*n* = 10) or W/W mice (*n* = 7). Statistical analysis was performed using a Mann–Whitney test. **(F)** Representative plot and frequency of integrin $\alpha4\beta7^+$ cells on effector ($CD62L^-CD44^+$) $CD4^+$ T cells isolated from MLN of 12wo +/+ mice (*n* = 10) or W/W mice (*n* = 7). Statistical analysis was performed using a Mann–Whitney test. **(G)** Serum cytokine levels from 12wo +/+ mice (*n* = 6), or 5 and 12 wo W/W mice (*n* = 3-3-63-66/group). Data are from more than three independent experiments. Groups were compared using a Kruskal–Wallis test with Dunn's multiple comparisons correction. *P < 0.05, **P < 0.01, ***P < 0.001, ****P < 0.0001.

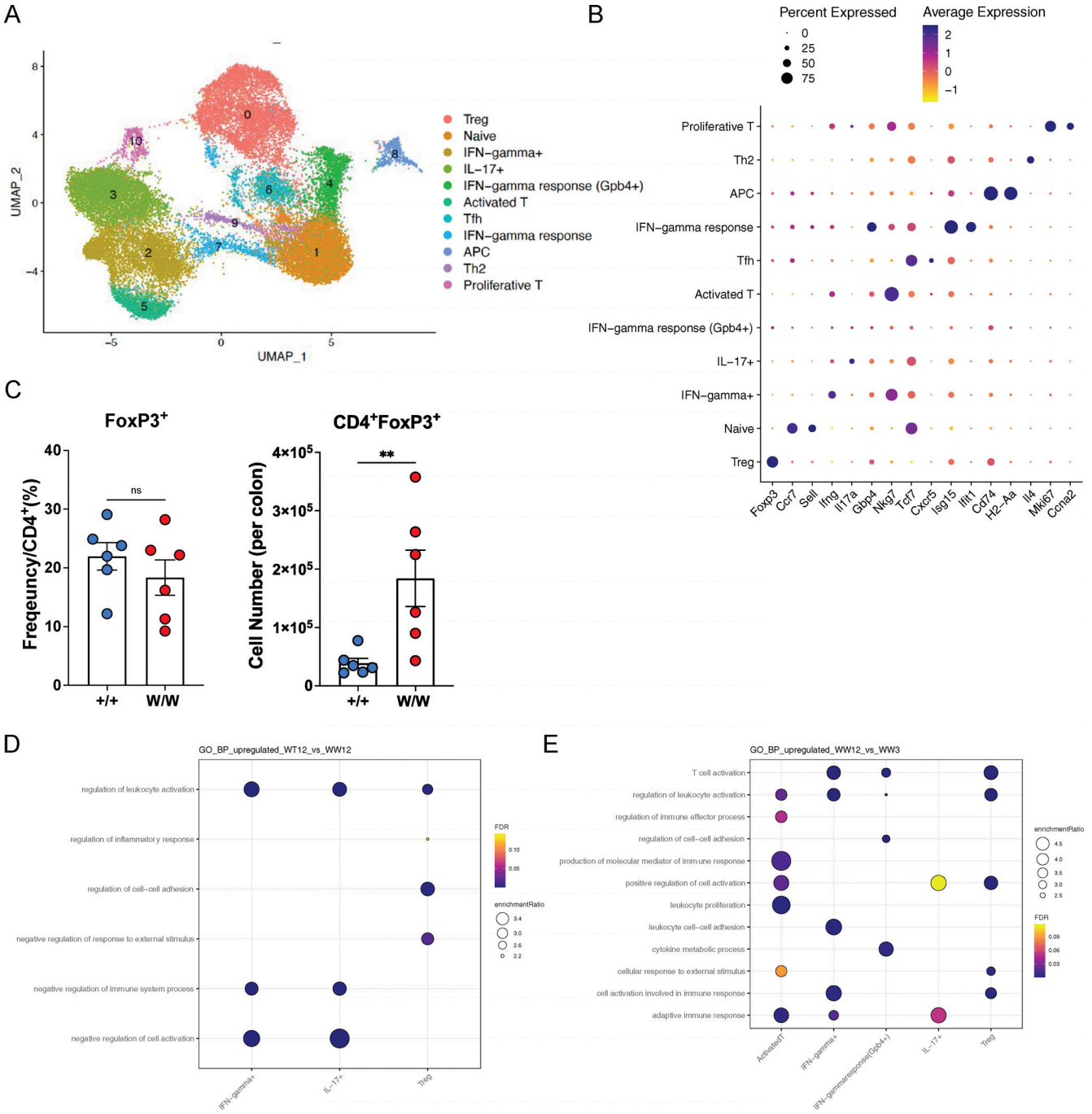

Figure S3. **scRNA-seq of LP CD4⁺ T cells in *Rag1*$^{w/w}$ (W/W) and wild-type (+/+) mice.** Total CD4⁺ T cells were sorted from the colonic LP of littermate +/+ or W/W at 3 and 12 wk of age and analyzed by scRNA-seq. Single-cell samples were obtained from four to five pooled mice/group. **(A)** The Uniform Manifold Approximation and Projection (UMAP) plot shows the expression profile of CD4⁺ T cells. Colors represent cells clustered together on the basis of similarity of global gene expression. **(B)** Dot plot shows percent and average expression of selected genes in each cluster. **(C)** Frequency and absolute count of CD4⁺FoxP3⁺ cells in the LP of +/+ or W/W at 12 wk of age (n = 6/group). Statistical analysis was performed using a Mann–Whitney test. **(D and E)** Selected gene ontology (GO) biological process terms enriched among gene sets differentially regulated (with >50% fold change and false discovery rate [FDR] = 0) in a cell type–specific manner between W/W and +/+ mice at 12 wk of age (D) and between W/W mice at 12 and 3 wk of age (E). The color of each circle represents the FDR value of the enriched GO term, whereas the size of each circle is proportional to the enrichment ratio, which is the number of differentially expressed genes associated with the GO term normalized by the number of such genes that one can encounter by random chance given the size of the total gene set in the GO database. Data are from at least two independent experiments. **P < 0.01.

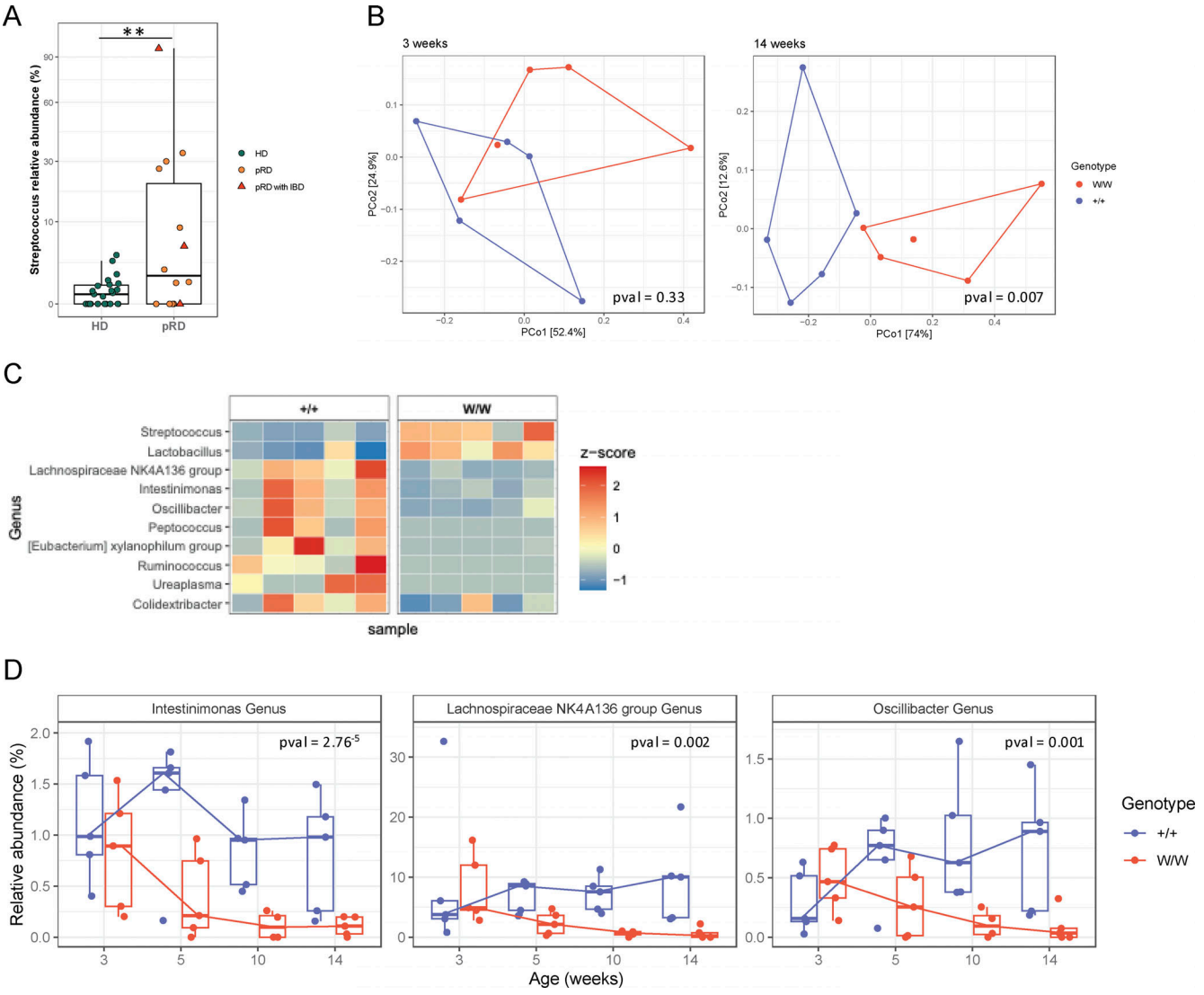

Figure S4. **Composition and diversity of fecal microbiota in W/W and wild-type mice. (A)** Relative abundance of *Streptococcus* in human fecal microbiota from healthy donors (HD, *n* = 23) and patients with pRD (*n* = 15). Significance was determined by a Kruskal–Wallis chi-squared test. **(B)** Principal coordinate plots show beta diversity using the Bray–Curtis metric of fecal microbiota from wild-type (+/+) or *Rag1*$^{w/w}$ (W/W) mice collected from isolated mice at 3 and 14 wk of age (*n* = 5/group). **(C)** Top 10 differentially abundant genus in the fecal microbiota of +/+ or W/W mice collected from isolated mice at 14 wk of age (*n* = 5/group). Significance was computed from the linear mixed-effects model ~Group + (1|SubjectID) using the MaASLin2 R package. **(D)** Relative abundance of *Intestinimonas* genus, *Lachnospiraceae* genus, and *Oscillibacter* genus in the fecal microbiota of +/+ or W/W mice collected from isolated mice at 3, 5, 10, and 14 wk of age (*n* = 5/group). Significance was computed from the linear mixed-effects model ~Group + (1|SubjectID) using the MaASLin2 R package. Data are from at least two independent experiments. **P < 0.01. HD, healthy donors.

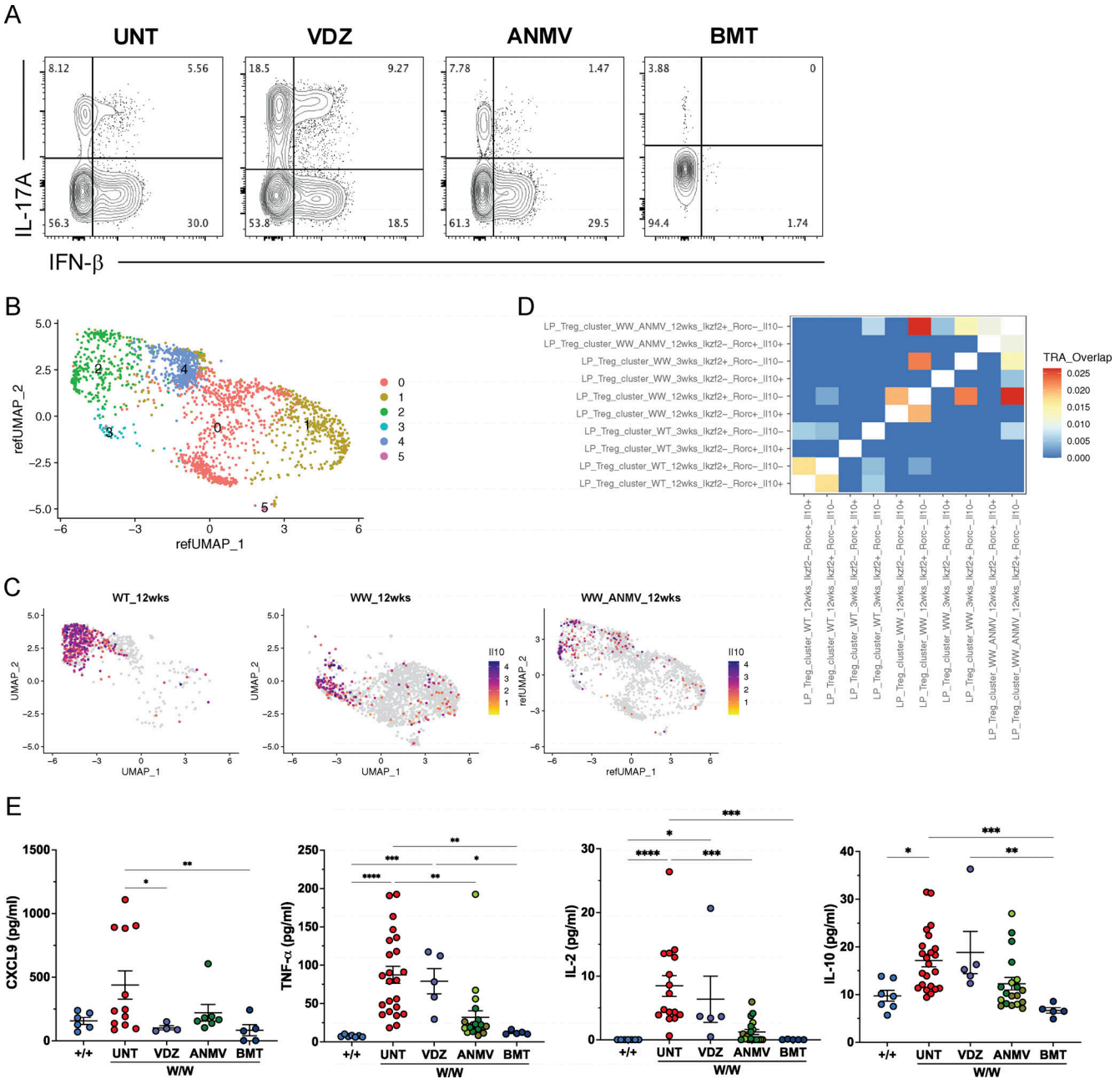

Figure S5. **Effects of various treatment modalities on intestinal and systemic inflammation, and on TCR repertoire composition. (A)** Representative plots of cytokine production by Th cells after restimulation gated on live CD45⁺CD90.2⁺TCRβ⁺ CD4⁺Foxp3⁻ isolated from *Rag1*$^{w/w}$ (W/W) mice untreated (UNT), or treated with VDZ, antibiotics (ANMV), or BMT. **(B)** Projection of Tregs from W/W mice treated with ANMV onto the UMAP coordinates derived from wild-type (+/+) and untreated W/W mouse (12 wk) Tregs. **(C)** Feature plots show single-cell gene expression levels of *Il10* projected on the Treg UMAP from +/+, untreated W/W, and ANMV-treated W/W mice. **(D)** Heatmap shows TRA overlap among different Treg subsets from +/+ mice, W/W mice at 3 and 12 wk of age, and ANMV-treated W/W mice. Single-cell samples were obtained from four to five pooled mice/group. **(E)** Serum cytokine levels from +/+ mice (n = 7), W/W mice untreated (UNT, n = 16), or mice treated with VDZ (n = 5), antibiotics (ANMV, n = 19), or BMT (n = 5). Data are from three or more independent experiments. Groups were compared using a Kruskal–Wallis test with Dunn's multiple comparisons correction. *P < 0.05, **P < 0.01, ***P < 0.001, ****P < 0.0001. VDZ, vedolizumab.